Tuebingen University

Diplomarbeit

Timing and Spectral analysis of the Low-Mass X-ray binary XB 1916-053

Author:
Alejandro Martinez Montero

Supervisor:
Dr. Santina Piraino
Pr. Dr Andrea Santangelo

A thesis submitted in fulfilment of the requirements for the degree of Physics Diplom

in the

Hochenergie Astrophysik Abteilung
INSTITUTE FOR ASTRONOMY AND ASTROPHYSICS

October 2014

alejandro.martinez@astro.uni-tuebingen.de

Declaration of Authorship

Hiermit erklaere Ich, Alejandro Martinez Montero, dass Ich die vorliegende Diplomarbeit mit dem Titel , 'Timing and Spectral analysis of the Low-Mass X-ray binary XB 1916-053' selbstaending verfasst und dabei keine anderen als die angegebenen Quellen und Hilfmittel benuzt habe:

Signed: _____

Date: _____

"There is a philosophy that says that if something is unobservable – unobservable in principle – it is not part of science. If there is no way to falsify or confirm a hypothesis, it belongs to the realm of metaphysical speculation, together with astrology and spiritualism. By that standard, most of the universe has no scientific reality – it's just a figment of our imaginations."

Leonard Susskind

Zusammenfassung

Röntgendoppelsternsysteme sind astronomische Objekte der Hochenergieastrophysik, die im letzten Jahrhundert zum ersten Mal entdeckt wurden. Durch die schnelle Entwicklung mehrerer Röntgenteleskope in den letzten Jahren ist die Erforschung dieser Systeme erleichtert worden. Bei der hier besprochenen Quelle handelt es sich um eine sogenannte Atoll-Quelle, ein Röntgendoppelsternsystem, das aus einem schwach magnetisierten Neutronenstern und einem massearmen Begleitstern besteht und eine schwache Leuchtkraft besitzt $\left(< 10^{37} erg\right)$. Wegen ihrer Besonderheiten sind Beobachtungen von Atoll-Quellen schwierig und viele ihrer Eigenschaften sind bis heute noch sehr umstritten.

Die hier untersuchte Quelle weist charakteristische Leuchtkraftabschwächungen, sogenannte Dips auf. Sie befindet sich auf 60 - 80 Inklination gegen*ü*ber der Erde.

Diese Diplomarbeit beschäftigt sich damit, sowohl spektrale als auch zeitliche Analysen dieser Quelle durchzuführen, um ein besseres Verständnis ihres Verhaltens zu bekommen und die existierenden theoretischen Modelle und die Ergebnisse früherer Studien zu verifizieren. Insbesondere werden Emissions- und Absorbtionsmuster in Dip und Kontinuumssituation untersucht.

Au*β*erdem sollen spektrale Eigenschaften, unter anderem die Beobachtung von zwei Eisenlinien während dieser verschiedenen Zustäden nachgewiesen werden. Weiterhin soll das "Partial Covering" Modell für diese Quelle überprueft werden und eine zeitliche Analyse durchgefuehrt werden, um das "Banana-shape" zu verifizieren.

Um diese Untersuchungen durchzuführen, wurden die Daten der BeppoSAX-, MAXI-, RXTE- und Suzaku Beobachtungen des Röntgendoppelsternsystems XB 1916-053 analysiert. Dabei wurde eine spektrale Analyse des Systems durch Anpassung verschiedener theoretischer Modelle an die Beobachtungen von BeppoSAX und Suzaku unternommen, wobei zwischen Dip- und Kontinuumssituation unterschieden wurde. Ferner wurden Color-Color-Diagramme von MAXI- und RXTE/ASM Beobachtungen erstellt, um die zeitlichen Eigenschaften des Systems zu analysieren.

Unsere Analyse und die erzielten Ergebnisse werden in Kapitel 5 diskutiert in Kapitel 6 zusammengefasst.

Abstract

X-ray binary systems are among the most fascinating objects emitting in the high energy range. The source discussed in the thesis belongs to one of their subclasses, the so-called Atoll sources. It is a binary star system consisting of a weak magnetised neutron star and a low-mass companion star with a faint luminosity $\left(< 10^{37} erg\right)$. Due to their characteristics, observations of Atoll-sources are difficult and many of their properties are still controversial today.

The light curve of the investigated source shows characteristic luminosity attenuation, the so-called dips. It is located at $\sim 60^{o} - 80^{o}$ inclination with respect to the Earth.

This thesis deals with both spectral and timing analysis of this source performed to get a better understanding of its behavior and to verify the existing theoretical models and the results of previous studies. In particular, emission and absorption features were examined during dip and persistent state. Two iron lines during these different states were observed. Furthermore, the "Partial Covering" model for this source has been checked and a timing analysis has been performed to verify the "banana-shape" timing behavior in the color color diagram.

To perform these studies, the data of BeppoSAX, MAXI, RXTE and Suzaku observations of XB 1916-053 were analyzed. A spectral analysis of the system was made using various theoretical models in the BeppoSAX and Suzaku observations, distinguishing between dip and persistent state. Furthermore, Color-color diagrams modeled by MAXI and RXTE / ASM observations were created to analyze the timing properties of the system.

Our analysis is discussed in chapter 5 and summarized with the obtained results in chapter 6.

Acknowledgements

I would sincerely like to thank professor Andrea Santangelo for the support throughout these years and the opportunity he gave me by giving me the possibility to work at the Tuebingen research group.
I would also like to thank Santina Piraino as my supervisor for all the help throughout the whole thesis.
I would like to thank Eva Laplace for all her help, Slawomir Suchy for his corrections, Sara Saeedi for all her support and Gabi Warth.
I would like to thank Giuseppe Distratis, Heinz Lenhart, Daniel Gottschall, Stephan Hermanutz, Anne Saulin and Timo Krahl for everyday coffee break. Thanks to Daniel Maier, Florian Jetter, Chris Tenzer and the rest for friday football.

Contents

List of Figures

List of Tables

Chapter 1

Introduction

1.1 History

The Universe is a vast space which consist of innumerable celestial objects. The study of the Universe itself, and what it contains, is called astronomy. The fascination shown by humanity about astronomy can be traced back as far as humans stated to be interested in knowledge, and probably together with theology it is one of the eldest studies known to mankind. History had a tremendous influence in the nomenclature being used, through different faiths and traditions. In order to be able to appreciate astronomy in its entirety, it is meaningful to know its beginning and its journey through the history of humankind, as well as the most important actors involved in the acquisition of the wisdom that we make use of today.

In ancient years, by the absence of tools as telescopes, studies about the sky with naked eyes were conducted in Mesopotamia, China, Egypt and Greece. In this time, ideas about the nature and origin of the universe started to emerge.

The study of astronomy as a science began with the ancient Greeks. The first written trails of astronomy can be traced back to around 730 B.C. At that time, the first "scientific" study conducted was the envision of the constellations. In the ancient Greek society the study of nature was a broad subject, which included physics, philosophy and astronomy among sciences.

Thales of Miletus (624-547) [1], a Greek pre-Socratic philosopher, can be considered as the first real astronomer in history, as he made many scientific advances in the field. Besides many of his works in philosophy and politics, he suggested various theories about Earth, mainly about its shape, size, and how it was supported. In his hypothesis, the Universe consisted of a flat Earth surrounded by water. Apart from these theories, he could predict the dates of the solstices and he tried to measure the size of the Moon and

Earth.

The next most notable astronomer of the Greek Era was Anaxagoras (500-428 B.C.) [2]. He adopted the explanation of a flat Earth developed by Thales and extended it, with the model of a drum shaped Earth, fixed in vacuum. Among his ideas in astronomy, he also suggested the existence of an external sphere far away, which would have the stars fixed on it and would rotate around the Earth.

Around 400 B.C. astronomy made a step forward into modern science as mathematics started to be a part of astronomy. Part of the new efforts were mathematical models that tried to clarify celestial motion. The greatest contribution of Eudoxus [3] was the illustration of the first plausible planetary motion. In addition to this, he also wrote other works, like "Disappearance of the sun", possibly on eclipses and "Oktaeteris", where he debated an eight year lunisolar cycle.

Aristarchus of Samos (310-230 B.C.) [4] presented the first planetarium model with the Sun at the center. In "On the sizes and distances of the Sun and Moon" he placed the distance of the Sun at around 20 times further than the Moon, where in reality it is around 400 times. It was the first real attempt for a distance measurement of celestial objects. Ptolemaeus (140 A.D.) was then responsible for the conception of the Ptolemaic system, where each planet is moved by a system of two or more spheres [5].

Although during the Greek Era many advances were done in astronomy, this did not continue over time and science found itself stuck without any relevant development for many centuries.

The next astronomical revolution came during the Renaissance, starting with the mathematician and astronomer Nicolas Copernicus (1473-1543) [6]. He conceived what was later called the Copernican revolution, the formulation of the heliocentric model. This model removed the Earth from the center of the Universe and replaced it with the Sun. He published this theory in the book "On the Revolutions of the Celestial Spheres". In spite of the fact that it was mathematically easier than the Ptolemaic model, it remained unused for over 60 years. This book is considered as one of the major events in the history of science until this day.

After Copernicus came Tycho Brahe (1546-1601). Thanks to a substantial quantity of measurements and their higher precision, he could see several flaws in the Ptolemaic planetarium motion system with respect to the position of the planets. After him, Johannes Kepler (1571-1630) devoted himself to analyze data acquired from Tycho Brahe, when he was his assistant. He published "Astronomia Pars Optica", he focused on optical theory, where he introduced the inverse square law that governs the intensity of light and where, in addition, he discussed the apparent sizes of celestial bodies. His extensive scientific research reached its peak with "Astronomia Nova", discussing a ten year investigation of the motion of Mars and providing strong arguments in favor of the heliocentric theory. In this book, he exposed the two first laws of planetary motion

and the study of Mars' orbit. He made several conjectures about the laws of motion of planets, changing the circular orbits to elliptical [7].

Galileo Galilei (1564-1642), was a distinguished Italian physicist, mathematician and astronomer. He is well known in the world of astronomy for the observation of Jupiter's moons, made possible by the technological improvements at this time, notably the Galilean Telescope [7].

Furthermore, he was a vehement defender of the controversial Heliocentric model, which led to his conviction by the Inquisition for heresy. Issac Newton (1642-1727) introduced the world to modern physics through his well-known laws, where the physical cause for the shape of the orbits gravitation (De phylosophiae naturalis Principia Mathematica, 1687) [8].

Discoveries of new stars, nebulae and clusters emerged thanks to improvements on

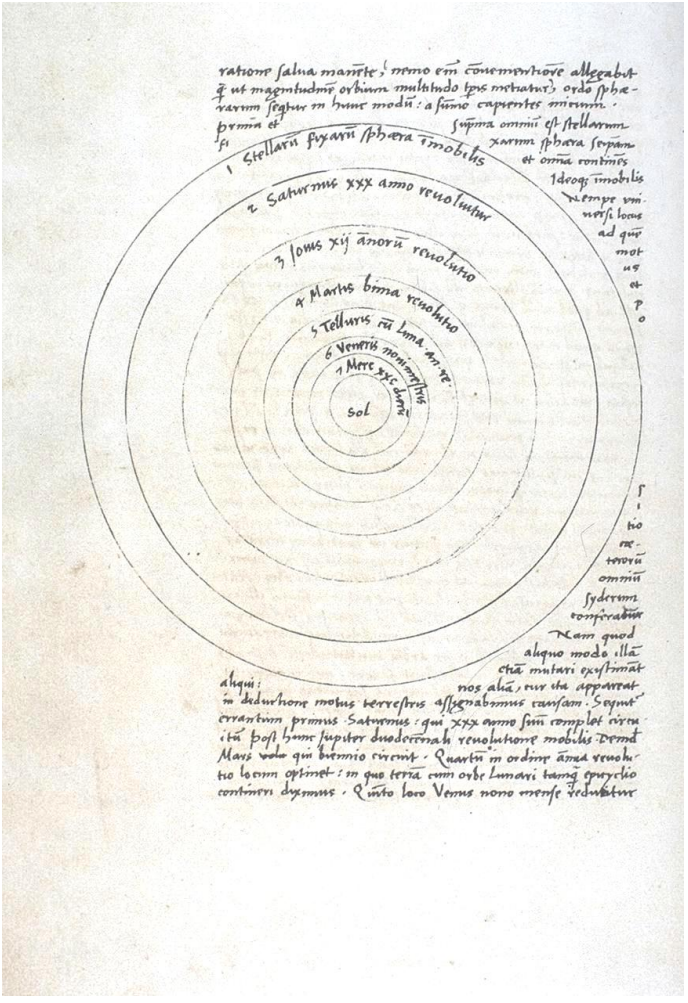

FIGURE 1.1: Heliocentric Model [6]

telescopes.

In the 18th and 19th century, thanks to Euler, Clairaut and D'Alembert, accurate predictions on motion of planets and the Moon were carried. This came through the development of the three-body-problem and the completion of the planet theory by Laplace towards the end of the century and which allowed Edmund Halley to successfully predict the orbit of a comet that eventually was named after him due to this discovery [9].
In the 19th century the gap between physics and astronomy got closer thanks to the discovery of the spectral lines coming from the sun. Charles Wheatstone made experiments with gases, observing spectral lines that corresponds to specific elements, obtaining the internal composition of the Sun. This work was extended by Joseph Von Fraunhofer who cataloged more than 600 lines [10].

1.2 Origin of X-ray Astronomy

Through the greatest part of the human history, mankind has always shown an interest in the study of the Universe, therefore being one of the oldest sciences known, but due to the lack of technology, the study of the Universe was only possible with optical telescopes and the understanding of the Universe was very constrained until recent years, where innumerable unique discoveries have been made with the development of new technologies and new telescopes that work in other energy ranges.
X-ray astronomy belongs to this part of the new astronomy that has been spread in the last 60 years, responsible for almost all the recent astronomy findings and presumably in the last century the field of physics which experienced the highest outgrowth. In recent years, thanks to X-ray astronomy, many parts of the sky that one century ago seemed to be empty, now are full with different and very interesting objects.
But first, what are X-rays? Like radio, microwaves, infrared, visible and ultraviolet, X-rays are a type of electromagnetic radiation. They have one of the shortest wavelength and together with Gamma rays they lie in the most energetic part of the electromagnetic radiation spectrum. As any other form of light, X-rays consist of photons. Since they have a very short wavelength, the use of frequency to characterize them is no longer convenient, but they are described with the energy that they carry. A typical range goes from few keV (kilo electron Volt) up to few hundreds of keV.
The first time that X-rays were observed was in a laboratory by the German scientist Wilhelm Conrad Roentgen at the University of Wuerzburg in 1895, while he was experimenting with vacuum tubes, for what he won the Nobel Prize in physics in 1901. This discovery opened a huge amount of new fields in physics and astronomy.
Many sources in our Universe are X-ray emitters, for example, our Sun emits X-rays, but it is important to notice that this is not its main type of emission. X-rays are emitted

in a much smaller quantity than in the optical wavelength.
A wide range of sources in our Universe apart from being X-ray emitters, have also X-ray emission as their main type of emission, making it necessary for us to use X-ray detectors in order to be able observe them.
The reason why high energy astronomy is a young research field is a technical one. In fact, X-ray observation on Earth is nearly impossible due to the photoelectric absorption of X-rays by the atoms and molecules of the Earth's atmosphere, which make Earth nearly opaque to high energetic electromagnetic radiation (see Fig. 1.2). This absorption happens to all electromagnetic radiation except for radio emission and optical light. Therefore it is no wonder that it was impossible to study X-rays from our Universe until balloons and satellites technology was developed, that is until very recently in our human history. The other main difficulty is that not only satellites are extremely expensive to build, but also very expensive to send on to orbit, as well as the detectors used, which need to be of a very high precision in order to be able to obtain a reasonable measurement. Needless to say, the maintenance of the satellite itself, which has to be assembled in order to survive for several years and ground based operations created only to acquire the data measured by the satellite are very expensive and require international efforts.

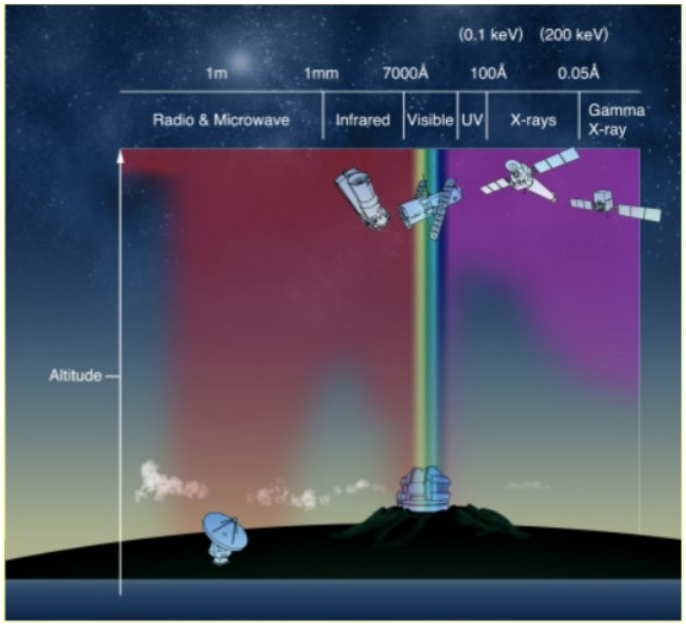

FIGURE 1.2: The Electromagnetic spectrum [11]

1.3 Missions

Due to the Earth atmospheric blocking of cosmic X-rays, the discovery of X-rays by Roentgen did not have a real impact on astronomy for quite some time. The first attempts were made sending balloons to high altitudes [12]. Only after the rocket technology surpassed the altitude of balloons, the science of X-ray astronomy could start. The first effort for astronomical X-ray detection was conducted by U.S. scientists commanded by Herbert Friedman in the 1940s. They arranged a Geiger counter in V2 rockets in order to measure solar X-rays, obtaining measurements of the order of 100 seconds [13].

In the 60s, new endeavors to study astronomical objects in the X-ray waveband started, when the Sun was the only known celestial X-ray source. This study was performed by a group at American Science and Engineering in 1962, commanded principally by the scientists Riccardo Giacconi and Bruno Rossi with a rocket flight carrying a small X-ray detector. It detected a very bright source in the constellation of Scorpius which they named Scorpius X-1, which is one of the brightest X-ray sources in the sky. They were awarded with a Nobel Prize in physics for pioneering contributions to astrophysics [14].

In the 1970s, there was an increase of the amount of X-ray astronomy satellites, creating a new era in High Energy Astrophysics [15].

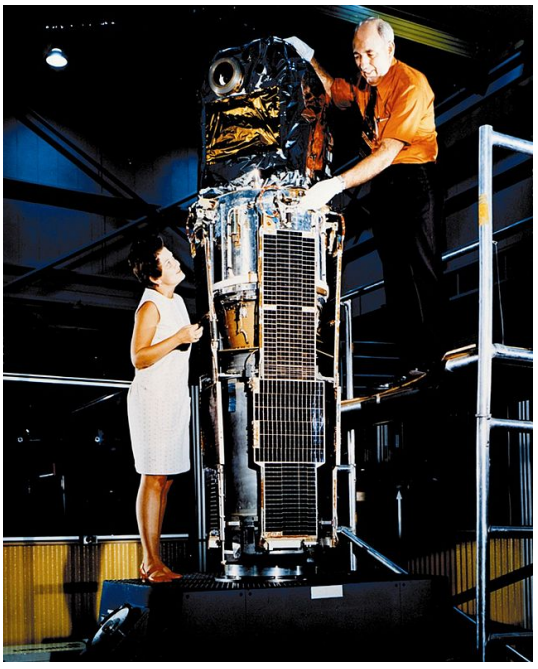

FIGURE 1.3: UHURU Satellite [16]

The first step in the measurement of X-ray celestial objects was made by the UHURU

Satellite. It was the first satellite launched specifically for the purpose of X-ray astronomy and started on the 12th of December 1970. The mission lasted for two years until March 1973.
The UHURU Satellite produced the first X-ray all sky survey, gathering more than 300 sources which were never detected before. It also located new types of sources, like binary systems, supernova remnants, Seyfert Galaxies and clusters of galaxies [17].
On the 12th of November 1978 NASA launched another satellite mission called HEAO-2, which was renamed Einstein. It was the first one of its kind to be a fully imaging X-ray telescope. Having an energy range of 0.2-20 KeV, its mission was to study soft X-rays, spotting faint sources and to image extended ones [18].
The European X-ray Observatory Satellite (EXOSAT), was a mission directed by the European Space Agency (ESA) [19]. It consisted of three instruments, covering an energy range of 0.5-50 keV. It was launched on May 1983. The duration of the mission was of three years after which a failure in the altitude control system caused the Spacecraft to lose its orbit. Beside previous X-ray astronomy missions, EXOSAT used a different orbit which was highly eccentric ($e = 0.93$) and had an inclination of 73 degree. This approach was done to maximize the observations of numerous sources that were concealed by the moon. Many observations in the X-rays regime were made by this satellite, including Active Galactic Nuclei (AGN), cataclysmic variables, white dwarfs, X-ray binaries and clusters of galaxies.
Throughout the following decades, the number of satellites being launched increased. Subsequently, the decade of the 90s became one of the most prolific in the study of the Universe in the X-ray wavelength. The Roentgen-Satellite (ROSAT), conceived as a German and UK partnership, was launched in 1990 and remained for 9 years. Its energy range was of 0.1-2.5 KeV and it spotted more than 10000 objects. The ROSAT mission made an all sky survey (RASS) which is considered as one of the largest X-ray catalog so far.
Another important satellite was the Rossi X-ray Timing Explorer Mission (RXTE). It analyzed the time structure of X-ray sources and had a broad energy range of 2-250 KeV in combination of three instruments. It was launched on 1995 and stayed operative until 2012.
Due to the increasing number of satellite missions in the beginning of the 90s, it can be considered that we are in a fruitful era of the X-ray astronomy. Plentiful number of missions have been launched since.
XMM-Newton is an X-ray Multi-Mirror Mission launched on December 10th 1999. This mission has been developed by (ESA) and it is the largest science satellite ever built in Europe. It carries 5 X-ray imaging cameras and spectrographs, and an optical monitoring telescope. Among other goals it tries to bring to light formation of galaxies and ranging from enigmatic black holes [20].

Another current mission is Fermi Gamma-ray Space Telescope, formerly known as GLAST. This mission launched on the 11 of June 2008 was developed by NASA with collaboration from government agencies in France, Germany, Italy, Japan and Sweden. It is capable of detecting photons at 300 GeV, and this mission will try to study Gamma-ray bursts, searching for evidence of dark matter [21].

A future mission will be Athena, one of the large ESA missions which is planned to launch in the 2020s. Its principal goals are to understand how ordinary matter assembles into large structures and also how black holes grow and shape the universe. Other missions like BeppoSAX, Suzaku and RXTE will be explained in more detail in the next chapters.

Chapter 2

Relevant Physical processes

All elements observed in the Universe can be explained by physical processes studied and theorized. In this chapter we will explain processes in the range of X-ray photons, produced at temperatures above 10^6 K.

2.1 Photoelectric absorption

2.1.1 Photoionization

It is the process consisting of the interaction of electromagnetic radiation with matter resulting in the dissociation of that matter into electrically charged particles. A simple example is the photoelectric effect. It is the major source of opacity in stellar interiors and stellar atmospheres. Consider a photon with energy $h\nu >> E_B$ where E_B is the binding energy of the electron in the atom, ion or molecule. The photon gets absorbed and an electron with E = $h\nu$ - E_B is emitted.

E_B is called absorption edge. Only photons with $h\nu > E_B$ can induce ejections from the energy levels. The energy of the absorption edge will depend on the energy level we are taking into consideration. In general, at X-ray wavelength the innermost shell, the K shell, is affected.

2.1.2 Fluorescence

After the electron has been ejected, a vacancy is left. The atom can then relax, i.e. a transition from a higher shell to the K shell takes place. A fluorescence photon is

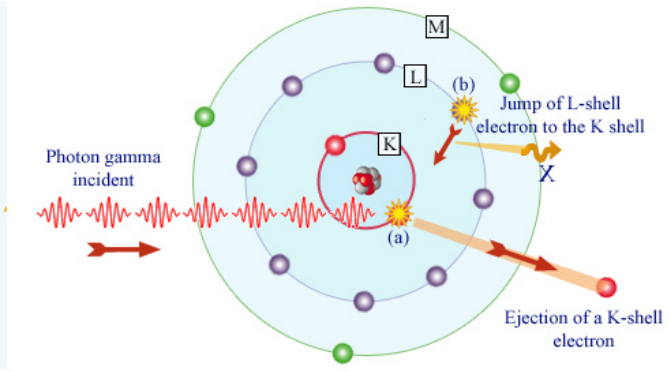

FIGURE 2.1: Photoelectric absorption [22]

emitted in the process.
Fluorescence photons get names according to the transitions they arise from:

- K_α : L $\rightarrow$ K
- K_β : M $\rightarrow$ K
- L_α : M $\rightarrow$ L
- L_β : N $\rightarrow$ L

In particular for iron the values of the transitions energies are:

- $E_{K_\alpha} = 6.403$ keV
- $E_{K_\beta} = 7.057$ keV

The primary electron can also ionize other atoms and create secondary electrons. It must also be stressed that the energy levels strongly vary with the ionization state and therefore the study of lines can give an indication on the ionization state of the plasma. Moreover, fluorescence lines are shifted to the ionization state of the atom.
For example, iron lines have energies:

- Fe XXV : $K_\alpha = 6.64$ keV
- Fe XXVI : $K_\beta = 6.93$ keV

Therefore the detection of the lines gives also an indication of the ionization state.

2.2 Blackbody radiation

A physical body is considered a blackbody when it emits and absorbs electromagnetic radiation in all wavelengths.
The ideal illustration of a Blackbody is to suppose it as a perfect absorber and emitter, as established by Kirchhoff [23]. Such Blackbodies do not exist in real life, yet this hypothesis can be used as a good approximation for establishing features and for a better understanding of different physical objects.

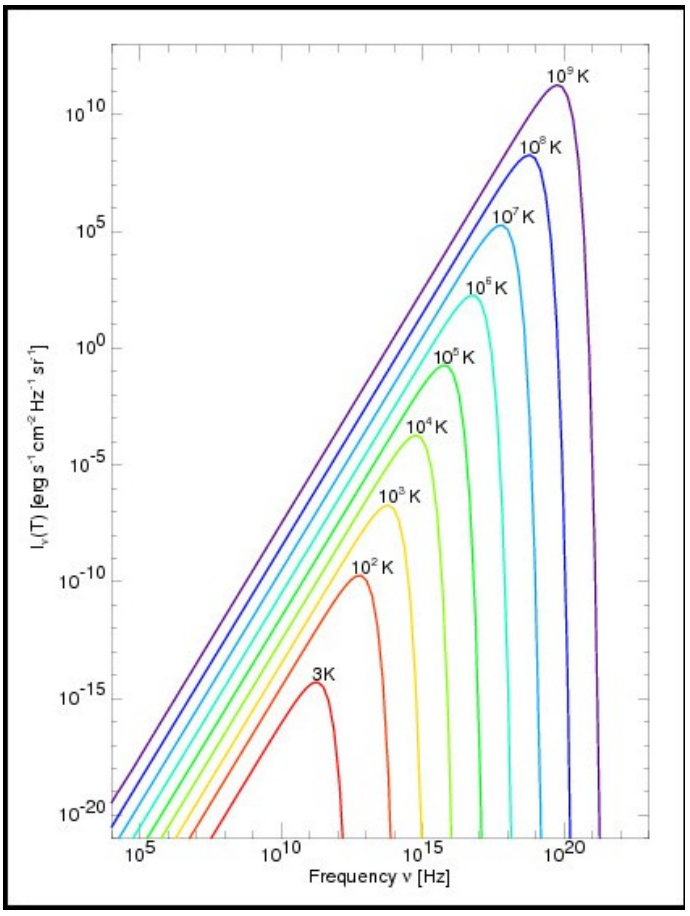

FIGURE 2.2: The Blackbody spectrum at different temperatures in terms of frequency [24]

Blackbody radiation has a specific spectrum and intensity that depends only on the temperature of the body.
Blackbody radiation was troublesome to be explained mathematically. The Wien displacement law, the Rayleigh Jeans law and the Stefan-Boltzmann law were the first attempts to physically explain it.
The Rayleigh Jeans law succeeds to illustrate the spectral radiance of electromagnetic radiation at low frequencies, but as long as the frequency increases, its predictions are

more and more inconsistent with observations. This problem is called the ultraviolet catastrophy.

$$u(\nu, T) = \underbrace{\frac{8\pi}{c^3}\nu^2}_{\textbf{Mode density}} \underbrace{k_B T}_{\textbf{Average Energy}} \tag{2.1}$$

Where k_B is the Boltzmann constant.
On the other side, the Wien displacement law only achieves to resolve the blackbody spectrum at high frequencies, but it is completely inconsistent at low frequencies.

$$u(\nu, T) = c_1 \nu^3 e^{-c_2 \frac{\nu}{T}} \tag{2.2}$$

with c_1 and c_2 as constants.
Stefan Boltzmann's law was obtained from Jozef Stefan in 1879 from measurements made by John Tyndall and Ludwig Boltzmann. He used thermodynamics to derive it in 1884. He considered an ideal heat engine with light as working matter instead of gas. This law describes the total energy radiated by a Blackbody per unit of surface area per unit of time and is proportional to the fourth power of the absolute temperature

$$F = \sigma \cdot T^4 \tag{2.3}$$

where F is the irradiance and with Stefan Boltzmann constant σ

$$\sigma = 5.67 \cdot 10^{-8} watt/m^2 \cdot K^4 \tag{2.4}$$

Planck's effort to try to solve this problem was to combine both (Wien and Rayleigh's) equations to check if he could obtain a new formula which could be consistent both at low and at high frequencies. He postulated that the oscillations in the cavity, given a specific frequency, would not give energy in a continuous way, rather in the form of packages or quanta in the following way:

$$E = nh\nu, \qquad n = 1, 2, ... \tag{2.5}$$

With this hypothesis, he was able to derivate and obtain the best formula to describe blackbody radiation. This result from Planck also correlates with the results obtained from the Stefan-Boltzmann equation when Planck's formula is integrated over all frequencies.

$$u(\nu, T) = \frac{8\pi}{c^3}\nu^2 \frac{h\nu}{e^{\frac{h\nu}{k_B T}} - 1} \tag{2.6}$$

Where

$$h = 6.63 \cdot 10^{-27} ergs : Plancks\ constant \tag{2.7}$$

$$k = 1.38 \cdot 10^{-16} ergK^{-1} : Boltzmann\ constant \tag{2.8}$$

Although Plancks conjeture fixed the problem, he was doubtful about the quantization of energy.
Blackbody radiation is a key part of astronomy. Many celestial objects emit Blackbody radiation, like hot stars, white dwarfs, neutron stars, accretion discs of neutron stars and black holes.

2.3 Bremsstrahlung

Bremsstrahlung is the modification of the acceleration of a charged particle generated by its deflection induced by another charged particle, generally an electron or an atomic nucleus (see Fig. 2.3). As the charged particle passes in the vicinity of the other charged particle, it is deflected by Coulomb interactions and loses kinetic energy. It will radiate a photon during this process due to the conservation of energy and momentum.

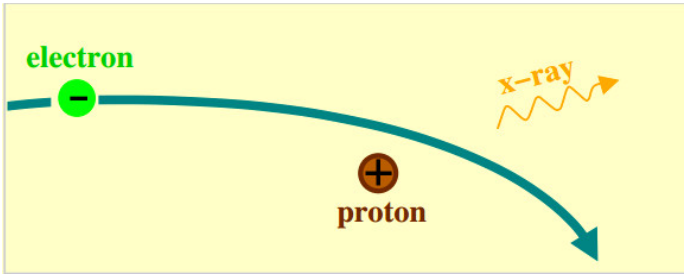

FIGURE 2.3: Bremmstrahlung [25]

Bremsstrahlung is frequently observed in hot gases, as the electrons collide with the nuclei due to their random thermal motions. Bremsstrahlung is one of the most common form of radiation in our Universe. It is produced at large in ionized gas, exhibits a continuous spectrum and can radiate in the X-ray wavelength if the energy of the charged particles is big enough. Good examples of these are the Interstellar Medium (ISM), clusters of galaxies and Supernovae Remnannts (SNR).

$$I(E) = (kT)^{-1/2}\, exp\left(-\frac{E_e}{kT}\right) \tag{2.9}$$

The exponential cut off appears because there are only exponentially few electrons at energies $\gg$ kT and that these are the only electrons that can radiate at $h\nu \gg kT$. Below kT is dominated by the exponential cut off, the spectrum is flat.

2.4 Compton scattering

Observation of the Compton effect is one of the most important experiments providing undeniable proof of the quantization of energy. The idea of quantization was first used by Planck, which helped him to achieve the derivation of his celebrated formula of the Blackbody radiation, however he was dubious about the authenticity of this idea and it remained very controversial until 1922, the year during which Arthur H. Compton conducted his experiment by radiating Graphite with X-rays.
The experiment of Compton consists of the collision of a high-energetic photon with an atom or molecule which can eject bound electrons from the outer shell. The wavelength of the scattered photon is shifted. This shift cannot be justified by using the classical wave theory. Consequently, the use of Planck's idea was advocated. Compton was awarded with a Nobel Prize in 1927. This effect can be taken as an example of an inelastic scattering, because the wavelength of the photon changes from before to after the collision.

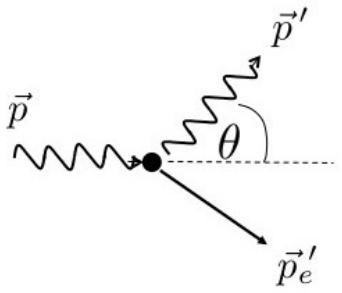

FIGURE 2.4: Compton scattering [26]

This process can be mathematically described by the equation 2.10:

$$\lambda^{'} - \lambda = \frac{h}{mc}\left(1 - cos\left(\theta\right)\right) \tag{2.10}$$

Where $\lambda^{'}$ is the wavelength after the scattering and λ is the initial wavelength. m is the rest mass of the electron, c is the speed of light, θ is the angle at which the photon is being scattered.
From this formula we can also extract the Compton wavelength λ_c which is equal to [26]:

$$\lambda_c = \frac{h}{mc} = 2,4.10^{-12}m \tag{2.11}$$

This is a quantum mechanical attribute of a particle. Its energy is the same as the rest mass energy of the particle.

$$\lambda_c = 2.426310 \cdot 10^{-12}m \tag{2.12}$$

There is a likehood for this effect to happen. This likehood was obtained in 1928 by Oskar Klein and Yoshio Nishina as one of the first results in quantum electrodynamics [27]. It is given by the differential cross section:

$$\frac{d\sigma}{d\Omega} \tag{2.13}$$

The Klein-Nishina formula for the differential cross section is:

$$\frac{d\sigma}{d\Omega} = \frac{r_\epsilon^2}{2}\left(\frac{E'_\gamma}{E_\gamma}\right)^2\left(\frac{E_\gamma}{E'_\gamma} + \frac{E'_\gamma}{E_\gamma} - sin^2\left(\theta\right)\right) \tag{2.14}$$

the equation 2.13 is the observed flux/incident flux.
Where E'_γ is:

$$E'_\gamma\left(\theta, E_\gamma\right) = \frac{E_\gamma}{1 + \left(E_\gamma/m_e c^2\right)\left(1 - cos\left(\theta\right)\right)} \tag{2.15}$$

2.5 Inverse Compton scattering

It is the scattering of ultra-relativistic electrons with low energy photons to higher energies, so that the photons gain energy at the expense of the kinetic energy of the electrons.
The energy of the scattered photon $\epsilon^{'}$ is given by:

$$\epsilon_1^{'} = \frac{\epsilon^{'}}{1 + \frac{\epsilon^{'}}{m_e c^2}\left(1 - cos\theta_1^{'}\right)} \tag{2.16}$$

where $\epsilon^{'}$ is the original photon energy and $\theta_1^{'}$ is the scattering angle.
Inverse Compton scattering can be described from the classical Thomson scattering if the energy of the photon in the centre of momentum frame of reference is much smaller than $m_e c^2$. This case is an elastic scattering, where the energy is conserved.
The electrons are assumed to be at rest and the photons lose energy through the scattering, however, when instead electrons are not at rest, the picture changes. As electrons move, they carry kinetic energy and therefore they will have much more energy than the photons. In this case the photons will gain energy transferred by the electrons. If

we take a gas of electrons doing Inverse Compton scattering with incoming photons as an example, this will give us as a product the cooling of the gas.
This process is observed in Astrophysics in the accretion discs of X-ray binaries and in the Cosmic Microwave Background (CMB) [28].

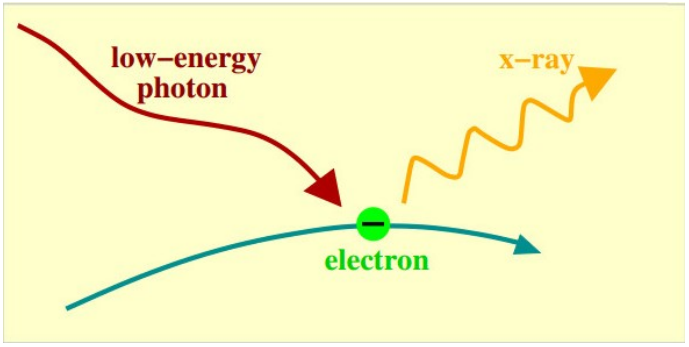

FIGURE 2.5: Inverse Compton scattering [29]

2.6 Comptonisation

From Compton scattering, the energy interchange between photons and electrons was shown. This is just a particular example of a more general process where electrons and photons of any energy interact. Comptonisation is the upscattering of low-energy photons by inverse Compton collisions in a hot electron gas. This effect has higher impact on very hot plasmas because the exchange of energy for each interaction is greater. As a requirement, the plasma must be rarefied so that other radiation processes such as Bremsstrahlung do not make an extra contribution to the system [30].
Restricting the comptonisation to the non-relativistic regime (for simplicity purpose), where $kT_e \ll m_e c^2$, the expression for the energy transferred to stationary electrons can be written in terms of the fractional change of energy of the photon per collision in the limit $\hbar\omega \ll m_e c^2$:

$$\frac{\Delta\epsilon}{\epsilon} = \frac{\hbar\omega}{m_e c^2}\,(1 - cos\alpha) \tag{2.17}$$

It can be approximated with a Thomson scattering, this means that the probability distribution of the scattered photons is symmetrical about their incident directions.

Chapter 3

Stars

3.1 Stellar Evolution

Stars in general, and the Sun particularly, have been and still are a primary subject of study in astronomy. Our Sun is a very close object to Earth and we receive its visible light in a much bigger quantity than any other celestial object in the Universe.
Many different factors have influence in the evolution and final remnant of a star like its luminosity, size or temperature. The one which has to be taken the most into consideration is the mass of the star. Knowing the mass of the star is already a good clue about its evolution and how it will end.
Stellar evolution is very complex and it undergoes through many different steps during the evolution of the stars. Particularly the origin and the death of stars are stages not well understood and still are under discussion.
The first stage of stellar evolution corresponds to the formation of the star. Dense clouds of gas inside molecular clouds collapse due to gravitation to form a gigantic celestial body, called protostar, that will become a star. Unfortunately not all the steps of the evolution of protostars are clear, yet the basic process is well understood. When the cloud of gas collapses, density increases in the interior of the star until nuclear reactions will begin in the interior of the protostar. This builds a force pointed outwards of the star preventing further collapse [31].
The Main Sequence stage is the most important one of the life of any star because the star will remain in this situation for the most part of its life. Radiation Pressure will be generated by Hydrogen fusion and this will be compensated by the action of gravity of the Star itself, until most of its Hydrogen is burned. The star will be in hydrostatic equilibrium. Stars in the Main sequence essentially have a fixed size that is a function of their mass. The more massive the star, the greater its gravitational pull inwards. This

in turn compresses the gas more [32].

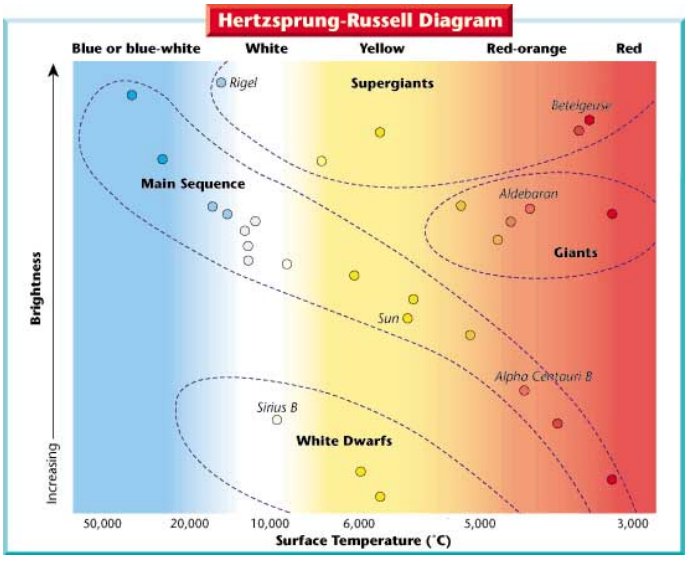

FIGURE 3.1: Hertzprung Russel Diagram [33]

Ejnar Hertzsprung and Henry Russel characterized the general behaviour of different stars and created a diagram in 1910. This diagram, called the Hertzsprung-Russel diagram (hereafter HRD), represents the relationship between the stars absolute magnitude, or luminosity, versus their spectral types and effective temperature. The creation and portrait of the different stars onto this diagram entail a major step towards the understanding of Stellar Evolution.

The main line in the diagram shows the Main Sequence, where a majority of the stars are located. Although there are some differences in the energy production of the stars, all of them rely of some type of Hydrogen fusion as the main radiation process.

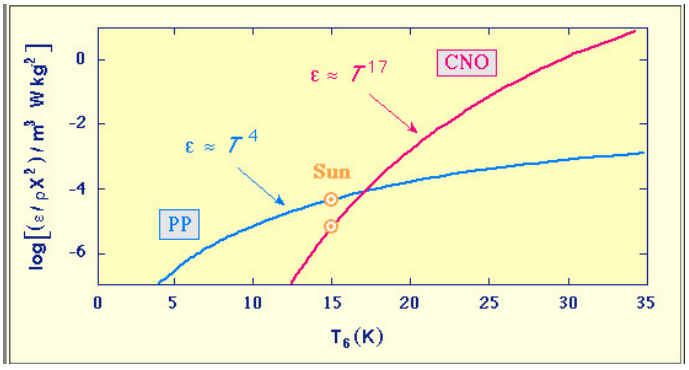

FIGURE 3.2: CNO and P-P cycle [34]

Nucleosynthesis refers to the production of nuclei heavier than Hydrogen. This happens inside stars by two main processes, which are the main way of energy production inside

a star. These two processes depend primarily on the mass of the Star and are called the Proton Proton chain (P-P chain) and the Carbon Nitrogen Oxygen cycle (CNO), respectively (see Fig. 3.2).

The P-P chain consists of the transformation of Hydrogen into Helium by nuclear reactions. There is a set of different possible reactions in order to accomplish this transformation, each one of them having a different probability [35].

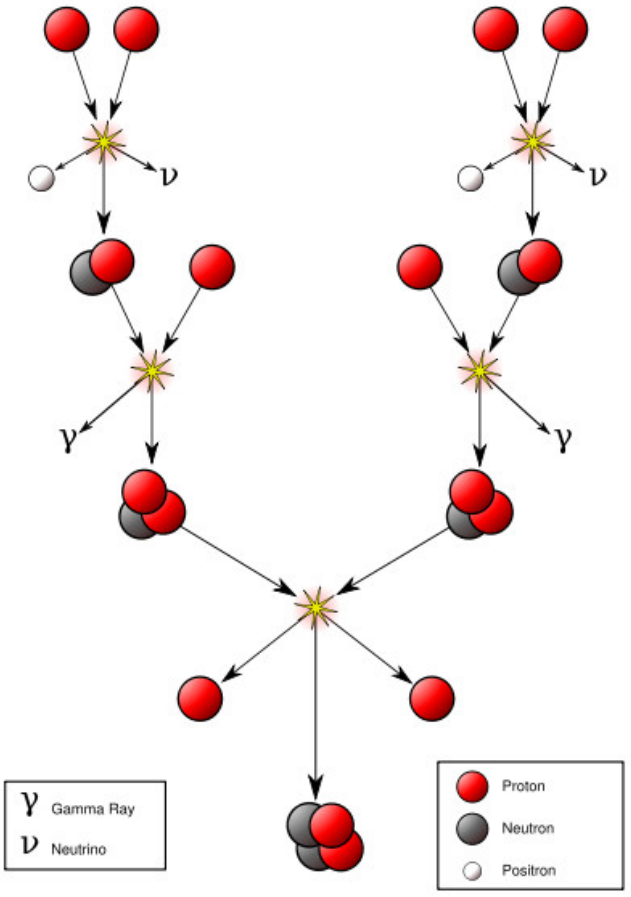

FIGURE 3.3: P-P cycle [36]

Unlike the P-P chain, the CNO cycle is a catalytic cycle. This CNO cycle takes over the predominance of energy production in stars with higher mass than 1.3 $M_{\odot}$. This process happens mainly in older stars, as you need C, N and O, which only occurs in stars with large mass.

The process basically consists of Carbon Nitrogen and Oxygen absorbing Hydrogen atoms, it creates unstable isotopes and finally after emitting photons producing a Helium atom. This process is much slower than the P-P chain [32].

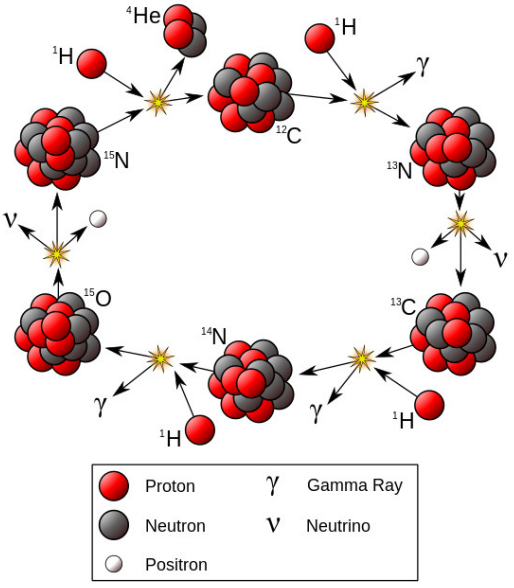

FIGURE 3.4: CNO cyclus [37]

The H-R diagram characterizes quite accurately all the various stages of Stellar Evolution, making it possible to identify the different types from their birth to their end products. One of the most basic properties that can be observed in a star is its luminosity. It is the total amount of energy emitted by the star per unit time. The luminosity can be measured with visible light or by measuring its total radiant energy. This is done by comparing the luminosity to the luminosity of the Sun:

$$L_{\odot} = 3.9 \cdot 10^{27} \quad Watts \tag{3.1}$$

Luminosity can be related to the absolute magnitude by the equation:

$$M_v = -2.5 \quad log\left(\frac{L_*}{L_{std}}\right) \tag{3.2}$$

Where L_* is the Luminosity of the object and L_{std} is the reference Luminosity. It is important to note that the measurement of the luminosity of an object requires the knowledge of its apparent magnitude and the distance of the object. The luminosity of stars in the Main Sequence is roughly proportional to their mass to the fourth power.

$$L \propto M^4 \tag{3.3}$$

[38]

3.2 End products of stellar evolution

After a star leaves its main sequence, it undergoes over a series of different stages. These stages are quite similar for all stars. Leaving the main sequence happens due to the loss of equilibrium between the two forces that keep the star together, radiation pressure and gravitational force. That means, that the amount of material to burn has changed. It normally happens after more than ten percent of the material in the star has been fused into helium. As helium is far more heavy than hydrogen, it will concentrate in the inner part of the star, being more dense in the interior than in the outside parts. The gravitational attraction cannot hold so closely the outer parts of the star, leading to its expansion and creating what is called a red giant.

3.2.1 White Dwarfs

White dwarfs are thought to be one of the possible end products of low mass stars, such as our Sun. After they have exhausting their nuclear fuel, they eject their outer layers as a planetary nebula and only the inner Helium core remain.
As the White Dwarf cannot undergo any fusion reaction, it has no source of energy and therefore it is not supported by the heat generated by fusion against gravitational collapse. Its only support is the electron degeneracy pressure, which makes it extremely dense. This collapse occurs when the core has reached a density of $\rho \sim 10^6$ g cm^{-3}.
Electron degeneracy pressure is a particular manifestation of the more general phenomenon of quantum degeneracy pressure. The Pauli exclusion principle disallows two half integer spin particles, fermions, from simultaneously occupying the same quantum state. The result is an emergent pressure against compression of matter into smaller volumes of space. The electron degeneracy pressure in a material can be computed as:

$$p_{deg} = \frac{\left(3\pi^2\right)^{2/3}\hbar^2}{5m_e}\left(\frac{\rho}{\mu_e m_u}\right) \tag{3.4}$$

Where $\hbar$ is the reduced Planck constant, m_e is the mass of the electron, ρ is the free electron density, $\mu_e m_u$ is the average particle mass per free electron μ_e. For a fully ionised iron $\mu_e = 2$ [39].
Electron degeneracy pressure will halt the gravitational collapse of a white dwarf if its mass is below the Chandrasekhar limit:

$$M_C = 1.44\mathrm{M}_\odot \tag{3.5}$$

The core has a temperature of T $\sim 2 \times 10^8$ K.
If the Star has a bigger mass, it cannot be supported by electron degeneracy pressure

and it will continue collapsing.
When a white dwarf is being formed, it is very hot, but as it does not produce energy, it will continuously radiate thermal energy away. This means that at the beginning, the star has a high colour temperature and redden over time. After it cools down it will no longer emit enough heat or light to be detected and most likely will become a black dwarf. Nevertheless the amount of time needed to become a black dwarf is estimated to be longer than the current age of the Universe and this is confirmed by the fact that no black dwarf has been observed yet. The oldest white dwarfs still radiate at temperatures of a few thousand Kelvin. [30]
White dwarfs have an approximately mass range from 0.17 to 1.33 $M_{\odot}$, although the vast majority being observed so far lie at a range of 0.5 to 0.7 $M_{\odot}$.
High densities, as in white dwarfs, can be achieved because the material consist of a plasma of unbound nuclei and electrons. There is therefore no obstacle to placing nuclei closer to each other than electron orbitals (the regions occupied by electrons bound to an atom) would normally allow.
Eddington however, wondered what would happen when this plasma cooled and the energy which kept the atoms ionized was no longer present. This paradox was resolved by R.H. Fowler in 1926, by an application of the newly devised quantum mechanics.
Since electrons obey the Pauli exclusion principle, two electrons cannot occupy the same state, and they must also obey Fermi-Dirac Statistics, also introduced in 1926 to determine the statistical distribution of particles which satisfy the Pauli exclusion principle. At zero temperature, therefore, electrons cannot all occupy the lowest energy state, or ground state; some of them have to occupy higher energy states, forming a band of lowest-available energy states, the Fermi sea. This state of electrons, called degenerate, means that a white dwarf could cool to zero temperature and still possess high energy.
Compression of a white dwarf increases the number of electrons in a given volume. Applying the Pauli exclusion principle, we can see that this will increase the kinetic energy of the electrons, increasing the pressure. This electron degeneracy pressure supports a white dwarf against gravitational collapse. It depends only on density and not on temperature. Degenerate matter is relatively compressible, this means that the density of a high-mass white dwarf is much greater than that of a low mass white dwarf and that the radius of a white dwarf decreases as its matter increases.

3.2.2 Neutron Stars

Neutron stars are one of the other possible end products of stellar evolution for stars with higher masses.

One year after the discovery of the neutron by Sir James Chadwick, Walter Baade and Fritz Zwicky in 1934 predicted the existence of the neutron star. [40]
A Neutron Star is a Stellar Remnant that is formed after a star's inner core stops burning material and its mass is greater than the Chandrasekhar limit. The star collapses in a type II, type Ib or type Ic supernova explosion (for further details about this classification see [41]). These types of end products are one of the dead stars known in the Universe.
The mass should also be smaller than the Tolman-Oppenheimer-Volkov limit (TOV). The TOV was computed in 1939 using the work of Richard Chace Tolman. They assumed that the neutrons in a neutron star formed a degenerate cold Fermi gas. From modern estimates the mass range is about 1.5 to 3.0 $M_{\odot}$.
A typical neutron star is composed primary of neutrons, with a radius of 20 km and a mass of 1.4 $M_{\odot}$. In 1967 the first pulsar candidate was observed, leading to the suggestion of the real existence of neutron stars. The surface temperature of a typical neutron star is around $6 \cdot 10^5$ K.
From the neutron stars being observed so far, the vast majority are in the category of pulsars. Pulsars are relatively young objects which rotate extremely fast.
Predictions say that we should expect more than a billion neutron stars in the Milky Way, but only around 2000 have been observed. Possible reasons for this difference in the amount predicted and the amount observed is that many of these neutron stars might be billions of years old, meaning that they have almost faded into invisibility because they lack the energy to power emissions at different wavelengths. [42]

The structure of a neutron star is one of the biggest puzzles of astrophysics. The outer layers of the neutron star are well understood, but as long as the density increases it gets impossible to understand how the matter is reacting because of the uncertainties in the equation of state of degenerate nuclear matter. The internal structure of a neutron star can be described in different layers:

1. The outermost layer, the surface layer, is a region with densities less than about $10^9 \cdot kg\ m^{-3}$. With this large density, the matter primordially consists of atomic polymers of Iron and due to the presence of strong magnetic fields, the atoms become cylindrical.

2. In this next layer, the density has a range of $10^9 < \rho < 10^{14} kg\ m^{-3}$. This region has matter with similar characteristics as the matter of a white dwarf, heavy nuclei forming a Coulomb lattice embedded in a relativistic degenerate gas of electrons.

3. The inner crust has densities between $4.3 \cdot 10^{14} < \rho < 2 \cdot 10^{17} kg\ m^{-3}$. It consists of a lattice of neutron-rich nuclei together with free degenerate neutrons and a

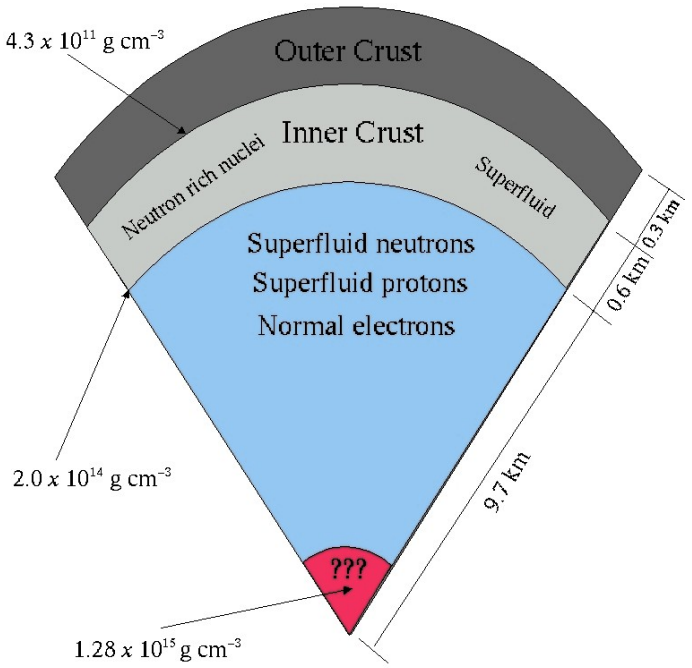

FIGURE 3.5: Neutron star internal structure [30]

degenerate relativistic electron gas. As the density increases, more and more of the nuclei begin to dissolve, and the neutron fluid provides most of the pressure.

4. The neutron liquid phase occurs at densities greater than $2 \cdot 10^{17} kg\ m^{-3}$. It mainly consists of neutrons with a small concentration of protons and electrons.

5. In the very centre of the neutron star, a core region of very high density may or may not exist. The existence of this phase depends upon behaviour of matter in bulk at very high energies and densities. Many of the models of stable neutron stars do not posses this core region, but it is certainly not excluded that quite exotic forms of matter could exist in the centre of some neutron stars [30].

In many ways, a neutron star may be thought of as one huge nucleus containing about 10^{60} nucleons. One of the remarkable consequences that neutron stars consists of matter in bulk at nuclear densities is that the inner regions of the neutron stars are likely to be super fluid and the protons superconducting [30].
A third form of a dead star would be a black hole. This star is far more dense than a neutron star, but further explanation about this object goes beyond the scope of this thesis.

3.3 X-Ray Binaries

X-ray binaries are composed by a compact object, normally a neutron star or a black hole and an optical companion, either a regular star or sometimes a white dwarf.
These type of systems are of a huge importance in astrophysics as they exhibit new physics and therefore they became one of the most interesting objects found in the sky in the recent decades. As they show new behaviour, many of their properties are still under study. Since the main type of radiation emitted by these systems is X-rays, they were not found until recently.

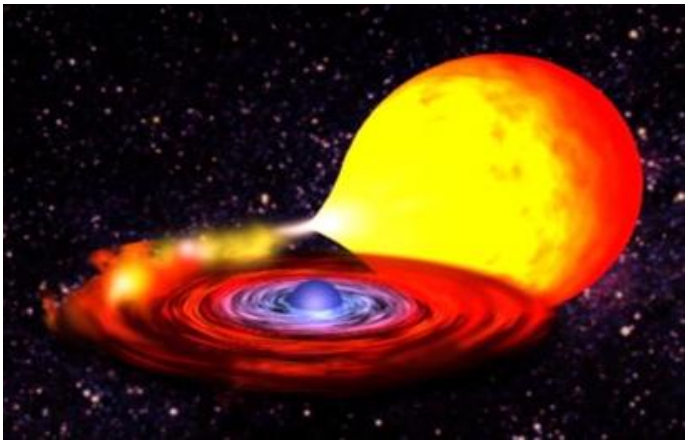

FIGURE 3.6: X-Ray binary [43]

The evolution of stars into a binary system is not fully understood and there are suggestions of how this can occur [44]. The most likeable explanation, among others, is the formation of two nuclei in a molecular cloud, giving birth to a binary system, each on of them accreting gas separately and evolving into stars.
Both stars follow the evolutionary stages of a normal star and eventually both reach the main sequence. The differences arise when the more massive star evolves faster than the less massive one. Their gravitational potential is by far more complicated than of an isolated star. The three-body-problem could be considered as an idealization to describe the system assuming that the stars are point masses [45].
Neutron stars are quite interesting objects and some of their features can be better observed in binary systems since there is no reason that can make us think that neutron stars would change their behaviour if they are part of a binary X-ray source or if they are isolated. Moreover, when they are part of a binary system, an enormous astrophysical bonus can be obtained. From these type of systems we can establish some of their properties, such as their masses, distances and physical environments.
Some properties from these binary systems were already known from observations in

other wavelengths already made with SAS-III, Ariel V, HEAO-1, Hackucho, Tenma and EXOSAT satellites. It can also be pointed out that the largest distribution of the bright X-Ray sources are situated towards the galactic plane, and in general in the direction of the centre of the galaxy [46].
The discovery of X-Ray binaries was obtained thanks to the observed pulsation in these sources (see Fig. 3.7).

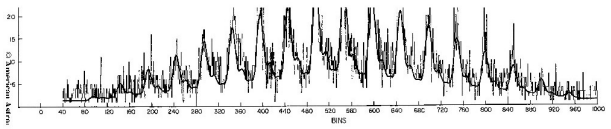

FIGURE 3.7: CenX-1 pulsation [47]

There are two main types of Binary sources known so far, High Mass X-Ray Binary (HMXB) and Low Mass X-Ray Binary (LMXB). We will discuss their differences in chapter 3.3.2 and in 3.3.3.

3.3.1 Accretion

Accretion can be described as the attraction of matter onto some object due to the influence of gravity.
Accretion is one of the most efficient sources of power in our universe. It can be seen specially in the study of X-Ray binaries, as a key process, from which we can unveil their masses and dimensions, contrary to what happens to other astronomical objects.
The process of accretion takes into consideration matter accreted for example by a star with mass M and radius R. If the matter falls onto the star in free-fall from infinity, it acquires kinetic energy as its gravitational potential energy becomes more negative. Considering a proton falling in from infinity, we can write:

$$\frac{1}{2}m_p v_{ff}^2 = \frac{GMm_p}{r} \tag{3.6}$$

[30]
The matter is rapidly decelerated when it reaches the surface of the star (r = R). If we assume that all the accumulated matter lies on the surface of the star, the kinetic energy of free-fall is radiated away as heat. Assuming rate at which mass is accreted onto the star is $\dot{m}$, the rate of dissipation of the kinetic energy at the surface of the star is:

$$\frac{1}{2}\dot{m}v_{ff}^2 \tag{3.7}$$

and hence the luminosity of the source is:

$$L = \frac{1}{2}\dot{m}v_{ff}^2 = \frac{GM\dot{m}}{r} \tag{3.8}$$

In the case of an X-ray binary, the physical process of accretion takes place by matter from one star transferred on to the other star leading to the emission of X-rays. This is one of the most efficient methods for generating high energy radiation.
The in-falling matter carries angular momentum, it falls towards the centre of a deep gravitational potential well, but the angular momentum impedes it to fall directly on to the compact object, therefore the matter starts to rotate around it forming an accretion disc.
Accretion is a physical process where gravitational energy is converted into kinetic energy. Rough estimations about the energy produced by accretion are given by the following formula:

$$E_{acc} = G\frac{Mm}{R} \tag{3.9}$$

This is the gravitational potential energy released E_{acc} when a mass m falls from infinity into a M mass body and a radius R. G is the gravitational constant. Taking standard values, as the mass of a neutron star M = $1.4M_{\odot}$, R_{NS} = 10 Km and m = 1 g for the in-falling matter, the estimated energy produced is:

$$E_{acc} \sim 10^{20} erg \tag{3.10}$$

This is an extremely efficient process. When it is compared to nuclear fusion, by the same amount of mass, 1g, the energy produced is:

$$E_{nuc} \sim 10^{18} erg \tag{3.11}$$

This is a good proof of the efficiency of this energy process.

3.3.1.1 Accretion Luminosity

From the gravitational potential energy released by accretion and with a M/R given, it is shown that the luminosity is

$$\frac{dm}{dt} = \dot{m} \tag{3.12}$$

$$L_{acc} = \frac{dE_{acc}}{dt} = \frac{GM}{R}\dot{m} = \frac{GM\dot{m}}{R} \tag{3.13}$$

The luminosity produced by a body with a given compactness depends on its accretion rate, $\dot{m}$.
At a certain luminosity, when the amount of matter accreted is too high, the number of photons produced will be so high that the radiation pressure will blow away the extra infalling matter. Then, the inward gravitational force is balanced by the outward transfer of momentum by radiation. That means that there is a maximum amount of luminosity that can be achieved by accretion. It is called the Eddington Luminosity.
Assuming an electrically symmetric accretion in steady condition and a fully ionized gas made by pure hydrogen, the gravitational force will be acting on electron-proton pairs. This is the inward force

$$F_{in} = \frac{GMm_p}{r^2} \tag{3.14}$$

The mass of the electron is negligible in this picture.
The radiation pressure is acting on the electrons with Thomson scattering, this is the outward force:

$$F_{out} = \frac{\sigma_T}{c}\frac{L}{4\pi r^2} \tag{3.15}$$

Leading to:

$$L_{edd} = \frac{4\pi GMm_p c}{\sigma_T} \sim 1.3 \cdot 10^{38}\frac{M}{M_\odot} ergs^{-1} \tag{3.16}$$

Accretion is only possible if gravitation is the dominant force, therefore:

$$L < L_{edd} \tag{3.17}$$

There are two main ways of mass transfer in a binary system. One is from stellar wind and the other is by Roche lobe overflow.

3.3.1.2 Stellar Wind

Stellar winds can be described as material ejected at high speed from stars, like protons, electrons and heavier elements. Stellar winds are characterized by a continuous flow of matter that can reach very high speed, even up to 2000 km/s [48].
Every star ejects matter through stellar wind at different speeds, rates and because of various causes, but hot massive young stars like O or B type can produce stellar winds up to billion times stronger than smaller stars. Consequently stellar wind is a much more important process in high mass stars than in low mass although they produce stellar wind too.
There are two important properties to consider in the stellar wind process. One is the

rate of mass loss $\dot{M}$, the other property is the velocity of the stellar wind at a large distance from the star, also called terminal velocity.
The mass loss rate can range from $\sim 10^{-10}$ to $\sim 10^{-6}$ $M_{\odot}/yr$.
The wind velocity is calculated by:

$$v\left(r\right) \sim v_{\infty}\left(1-\frac{R}{r}\right)^{\beta} \tag{3.18}$$

with $v_{\infty} \sim 2000$ km s^{-1} and $\beta \sim 0.5$ ... 1.0.
In binary systems, as we can see in figure 3.8, the compact object will accrete matter through stellar wind ejected from the massive star. Only a fraction of the ejected matter will be transferred to the compact object. It is assumed that the winds emitted by O or B type stars are isotropic.

Many of the observed X-ray pulsations have companions of early spectral type (O or

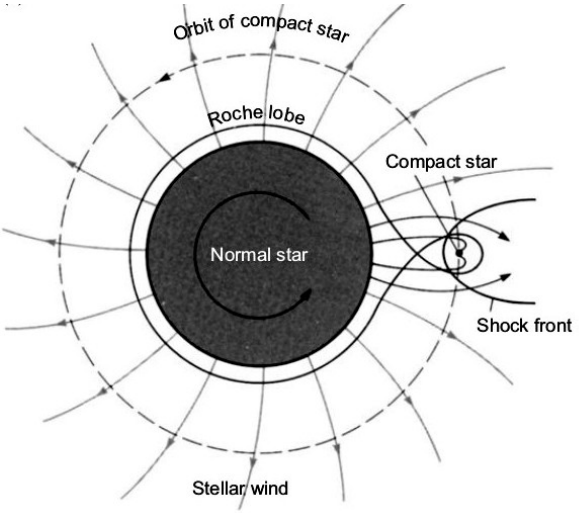

FIGURE 3.8: Wind Accretion [30]

B). Such system can be very luminous and many of the first galactic X-ray sources to be discovered (e.g. Cen X-3, SMC X-1 and Vela X-1) fall into this category. Early-type stars are known to loose mass in the form of a stellar wind, with mass loss rates as high as 1 - 6 $M_{\odot}/yr$. Hot, massive stars can produce stellar winds a billion times stronger than those of low-mass stars. Over their short lifetimes, they can eject many $M_{\odot}$ (perhaps up to 50% of their initial mass) of material in the form of 2000 km/sec winds. These stellar winds are driven directly by the radiation pressure from photons escaping the star. In some cases, high-mass stars can eject virtually all of their outer envelopes in winds. The result is a so called Wolf-Rayet star.

3.3.1.3 Roche Lobe

Roche lobe is another type of accretion method for X-Ray binaries. It takes place when the donor star fills its Roche lobe, following the stars evolution and expansion. When this happens, the matter exceeding the Roche lobe is no longer gravitationally bounded to the star and can be captured by the compact object through the inner Lagrange point.

In this type of system, there are five specific places called Lagrangian points. In these

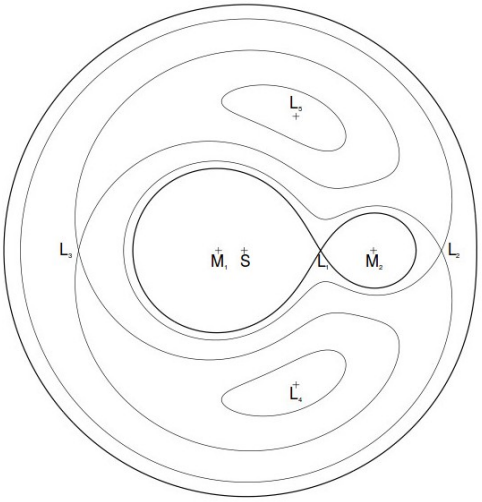

FIGURE 3.9: Roche lobe potential [49]

points the potential of all gravitational forces void each other, so if a body without any force reaches this point, it can remain in this position forever. From the picture, L_1 point is the point that lies on the line between the two masses of the system and therefore matter will flow through this point. As the system rotates due to gravitationally binding, the matter that passes through the Lagrange point carries a large amount of angular momentum and the matter will not fall into the compact object directly, instead it starts to rotate around it and eventually falls into the compact object, originating an accretion disc.

Apart from Roche lobe, stellar wind also takes place in low mass and/or late type stars, however as this process is not particularly strong in this case, the matter accretion will be accomplished by Roche lobe overflow. As well, it is assumed for these types of systems that the stars co-rotate. The equipotential lines comes from these assumptions. Close to each object, the gravitational force dominates the potential of the star, thus the surfaces are almost spherical.

The curved lines from the Roche lobe potential picture corresponds to $\phi(\vec{r}) = \text{constant}$, where rotating around the axis, closed equipotential surfaces are obtained. It has two

potential wells and five Lagrangian points.

3.3.2 HMXBs

A High Mass X-Ray Binary is a gravitationally bound system composed by a neutron star or a black hole as the compact object and a massive star, generally a O or B type, that is $> 5M_{\odot}$.
The more massive star evolves faster and reaches the end of its life first, after a few million years or so. It becomes a giant and the outer layers are lost to its companion. Then it explodes in a supernova, leaving behind either a neutron star or a black hole. This can disrupt the binary system, but if the star that exploded was less massive than its companion when it exploded, the systems will remain intact, though the orbits may be more eccentric. The companion star then comes to the end of its life and swells to form a giant. It then looses its outer layers onto the neutron star or black hole.

Properties	HMXBs
Donor Star	O-B (M$> 5M_{\odot}$
Population	I (10^7yr)
L_x/L_{opt}	0.001-10
X-Ray Spectrum	hard(kT $\geq$ 15 keV)
Orbital period	1 - 100 days
X-Ray eclipses	common
Magnetic field	Strong ($\sim 10^{12}$ G)
X-Ray pulsations	common (0.1 - 1000s)
Type I X-Ray bursts	absent
X-Rays QPOs	rare (0.001 - 1 Hz)

The material forms an accretion disc around the compact object, which heats up because of friction. This heating, combined with jets that can be formed by the black hole, cause the X-ray emission. Eventually the companion star comes to the end of its life, leaving a neutron star/black hole - white dwarf/neutron star/black hole binary, depending on the initial masses of the stars.
Cygnus X-1 is this type of X-ray Binary. It is bright in X-rays not only because of the accretion disc, but also because there is a corona which is much more powerful than the Sun's corona. As an example, Cygnus X-1 is 10000 times more powerful than the Sun, and most of it is powered by the gravitational pull caused by the black hole.

Its definition of high mass comes from the size of the optical companion of the system. In the case of a HMXB the optical companion is a type O or B Star, also a Be star or a blue supergigant.
HMXBs are easier to observe because the emission is dominated by the optical companion and they are very massive and luminous. The main method of accretion for these systems is with stellar wind. The optical companion ejects matter through stellar wind method, a fraction of the matter ejected is acquired by the compact object, radiating X-Rays as the matter falls onto the compact object. HMXBs are young objects, as the lifetime of such big optical companion is way shorter than smaller stars.

3.3.3 LMXBs

Low-Mass X-Rays binaries (hereafter LMXBs) corresponds to the binary system composed by a neutron star or black hole as the compact object and as the stellar companion a star with less than 5 $M_{\odot}$. The latter is typically a late type K or M star, or if the system exhibits a very short orbital period, a white dwarf.
As LMXBs have old stars in their systems (population II), they are believed to be ancient systems, many of them being found in the vicinity of the galactic bulge.
In most cases the main type of accretion method for this type of system will be through the Roche lobe overflow. As the donor star rotates around the compact object, the matter accreted carries angular momentum, and it will not be directly accreted but will start to rotate around the compact object, forming an accretion disc.

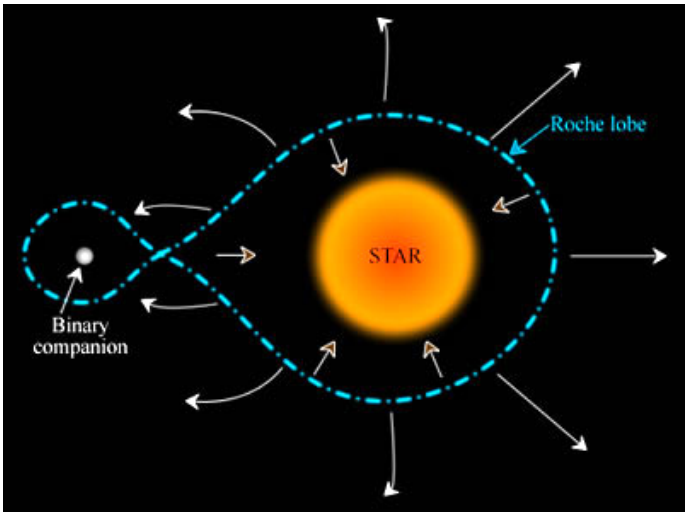

FIGURE 3.10: LMXB [50]

The gas in the accretion disc loses angular momentum through collisions, shocks viscosity and through the action of the neutron stars magnetic field. From all of these processes, the kinetic energy is converted into heat and is radiated in the form of X-Rays. The matter falls inwards getting closer to the neutron star and possibly starts to sink into the compact object at some point.

LMXBs are distinguished by having lower luminosities than HMXBs, $L \sim 10^{36}$ - 10^{38} $\frac{erg}{s}$. They are also identified by soft X-Ray spectra: kT $\leq$ 10 keV and hard tails can be observed up to 100 keV.

LMXBs usually exhibit orbital periods which go from minutes up to several days, X-Ray bursts have also been observed and in some cases display pulsations. Their neutron stars usually have lower magnetic fields than HMXBs, 10^{-8} - 10^{-10} G.

During the evolution of the binary system, it might happen that at some point one of the stars may increase its radius or the separation between both stars shrink, to the point that the optical companion reaches the Lagrange point L_1, which allows the Roche lobe accretion to start, removing the outer layers of its envelope.

The evidence of their binary nature is rather not obvious.

The accretion disc is believed to be responsible for the X-Ray luminosity produced, where its vast majority comes from the inner region. Although this might be the main source for X-Ray emission, other additions are to be taken into account. As observed in eclipsing systems, The X-Ray source is not completely occulted, giving the evidence for the existence of an accretion disc corona surrounding the system, which fullfills a fraction of the Roche lobe of the neutron star. As it is only a fraction of the total luminosity, it is unclear if it can be scattered radiation from the compact source or if it is a hot corona. Either way it results from heating by the X-Ray source or from instabilities in the accretion disc.

Thickening of the accretion disc can also be an addition to the luminosity. Its origin is not well understood. As a possible explanation, it can be that the stream of plasma accreted through the Lagrangian L_1 point might be wider than the accretion disc thickness at the point where they encounter each other. From this, streams of material will join over the disc until they reach centrifugal equilibrium.

Properties	LMXBs
Donor Star	K-M or WD (M< $5M_{\odot}$
Population	II (5-15 10^9yr)
L_x/L_{opt}	100 -1000
X-Ray Spectrum	soft (kT $\leq$ 10 keV)
Orbital period	10 min - 10 days
X-Ray eclipses	rare
Magnetic field	Weak ($10^7 - 10^8$ G)
X-Ray pulsations	rare (0.1 - 100s)
Type I X-Ray bursts	common
X-Rays QPOs	common (1 - 1000 Hz)

3.3.4 Atoll and Z sources

Within the LMXB category, the sources with weakly magnetized neutron stars are divided into Atoll and Z sources. Both types exhibit soft spectra and the majority do not exhibit any pulsation. Together, the two groups encompass many of the LMXBs that are persistently brighter than 100 μJy.

Atoll and Z sources differ to each other in their luminosity, for example Atoll sources corresponds to low luminosity systems $< 10^{37}$ erg s^{-1}. These differences can be portrayed by Color-Color Diagrams (hereafter CCDs) and the Hardness-Intensity diagram (hereafter HIDs) including their timing properties and variations. [51]

A CCD is made of a soft colour on the X axis and the Hard colour on the y axis. An X-Ray colour or "Hardness ratio" can be defined by the following formula:

$$color = \frac{CR_{upper\ energy\ band}}{CR_{lower\ energy\ band}} \tag{3.19}$$

The Count Rate (hereafter CR) corresponds to the CR measured from the light curve in a given energy band. The energy ranges used are not fixed because they differ with each satellite. In any case its typical width corresponds to a few keV. The soft colour corresponds to the colour in low energy range, and the hard colour in a higher energy range.

Z sources

- The CCD of a Z source displays a Z shape, that is easy to identify (hence their name). This diagram traces the states of the source in time scales from hours up

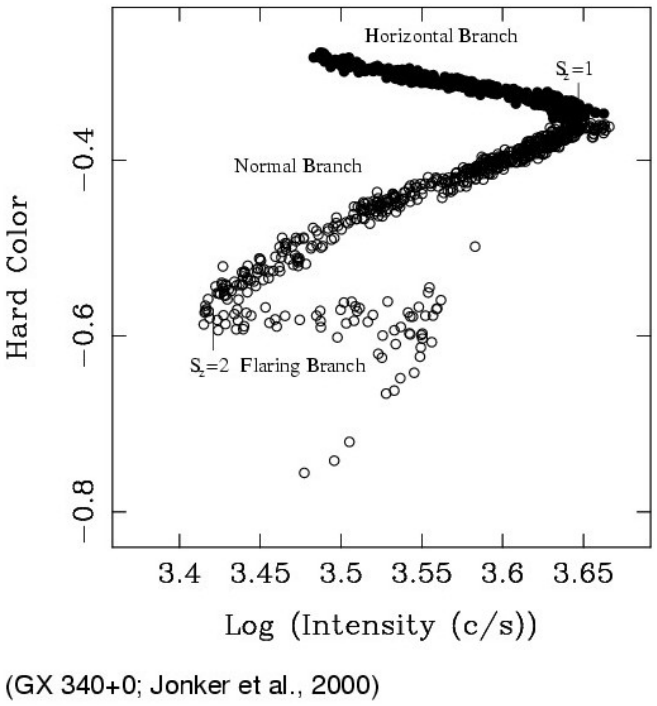

FIGURE 3.11: CCD of a Z source [52]

to several days. The Z shape is divided in distinguishable parts that conform the Z shape: The Horizontal branch, the Normal branch and the Flaring branch (see Fig. 3.11).

- Z sources are high luminous LMXBs sources, higher than Atoll sources and close to the Eddington luminosity L_{edd}.
- A characteristic of the Horizontal branch is the oscillations observed in the 20-50 Hz range, named "Horizontal Branch Oscillations" (hereafter HBOs) plus a strong variability present and also Quasi Periodic Oscillations.
- The variability in the Normal branch is weaker than in the horizontal branch
- The Flaring branch corresponds to the lowest part of the CCD. This branch is mostly thermal and was named after the flares observed in Sco X-1
- The intensity is described by the S_z factor. This factor changes from one part of the spectrum to the other [53].

Although the Z shape in characteristic for these types of sources, this shape might get severely deformed or shifted, because of the source or due to a different range of colour bands used.

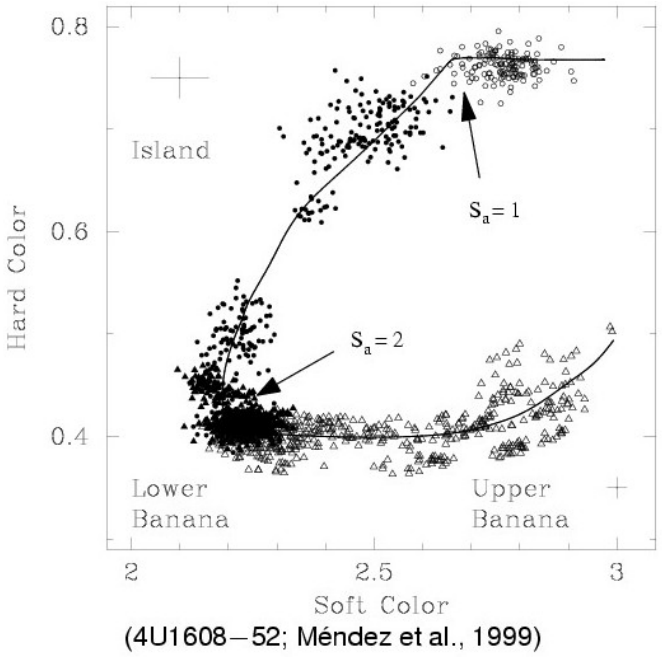

FIGURE 3.12: Color color diagram Atoll source [54]

Atoll sources

- Atoll sources have a different shape in their representation on the CCD than Z sources due to among other characteristics, their lower luminosity. It resembles a pacific island. The intensity parameter is represented with S_a, dividing its characteristic regions from the lower to the upper part.
- The Banana State: It shows a high luminous state and the variability is dominated by the low frequency noise. The banana shape is also divided into lower banana and upper banana, where the upper banana describes a higher spectra behaviour than the lower part.
- The Island state: This state represents a lower luminous state than the banana shape where the variability is dominated by the high frequency noise.
- Distinctive luminosities are of the order of 0.01-0.2 L_{edd}, but some sources may show higher luminosities [53].

Atoll sources are variable sources, therefore they appear in different parts of their CCD depending on the time of observation, as they vary on time-scales that go from hours to weeks. If the source is observed long enough, the movement along the diagram will be sequential, that means that if it is first observed in the upper banana, it will go to the lower banana, then to the island and finally go back without jumping from one state to

the other randomly.
The time spent on each region is different. Being in the island, it can stay there from a few days to several weeks. On the contrary, in the banana, the source normally only stays there between a few hours and a few days. Anyhow, these time-scales varies with each source and all of these time variability depends on the individual source luminosity variations.

3.3.5 Dips and Eclipses

Two important characteristics observed in X-Ray binaries are eclipses and dips. An eclipse happens when the observed object is temporarily obscured. This can occur by having another body between it and the observer. On the other hand, a dip is a periodic obscuration of the X-Ray emitting region by a structure located in the outer regions of a disc particularly believed to be the impact region of the accretion flow from the companion star.
As the different LMXBs are observed at different angles, in some of them eclipses and/or dips are observed. Although LMXBs are well studied systems, it is rather uneasy to verify their binary nature. Dips and eclipses are key points for this corroboration.
Systems observed face-on lack of dips and eclipses. They give their brightest and most luminous states to the observer and the compact object is not occulted at any moment. In this case the binary nature of the system is not easy to observe as the movement of the system is less clear.
At large inclination angles, the system's behaviour will display other features. At angles of 60-75 degree on inclination, dips will be shown in the light curves periodically. As dips are not produced as in the case of eclipses, by a body between the observer and the source, it is believed that these dips are caused by the material streamed into the accretion disc when it passes through the line of sight [55].
Eclipses are produced at large angles, starting at 75 degree of inclination. It is presumed that the objects co-rotate, so as they rotate around, from the observer point of view, the compact object hides itself behind the companion once every orbital period, staying in line of sight. From this behaviour, a decrease in the X-Ray intensity observed over time is displayed. It can produce either total or partial eclipses, depending on various factors, like the size of the object, the inclination angle, upon the disc geometry and so on.
A studied system observed at a large inclination angle has either a periodic reduction of the X-Ray emission or shows attenuations, leading to the verification of dips and eclipses by observing their light curves.

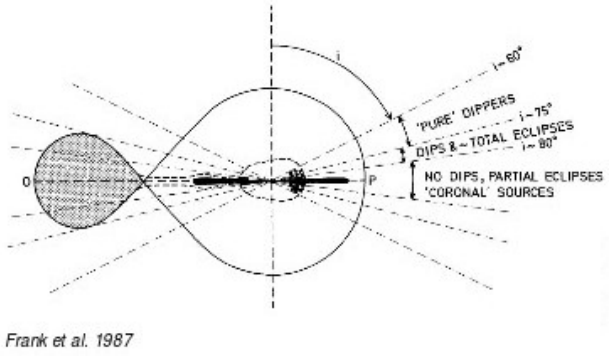

FIGURE 3.13: Dips and Eclipses [56]

3.3.6 X-Ray Bursts

An X-ray burst is described by the sudden rise of the luminosity of an XRB, lasting for a couple of seconds or even up to few minutes followed by a slower decay corresponding to cooling in the decay phase. Bursts may only happen in a small amount of LMXBs. Their origin comes from thermonuclear flashes in the matter accreted directly on the surface of a neutron star. The energy of the photons shapes the burst by displaying much shorter decays at high energies than at low energies. This energy dependence corresponds to a softening of the burst spectrum during the decay, which is the result of the cooling of the neutron star's photosphere. Burst intervals can be regular or irregular on time scale of hours to days. burst activity can stop as well for periods from days to months. In some cases, a relation has been observed between the burst profile and the persistent emission.

X-ray luminosity increases above a level of 10^{37} erg s^{-1} [57].

An X-Ray burst is represented by an energy/time dependent spectrum. It can be well modelled by a blackbody spectrum. During these bursts, the luminosity increases to be close to the Eddington limit. It is presumed that during it, the atmosphere of the neutron star expands due to the radiation pressure, possibly through the formation of a stellar-wind outflow of material from the neutron star. After that the luminosity decreases below the Eddington limit and the photosphere contracts [58].

Chapter 4

Satellites

X-ray satellites are used for the study of the Universe in the X-ray and Gamma ray range. Due to the photoelectric absorption of high energy photons in the atmosphere, satellites are the only way to study extraterrestrial X-rays.
Satellites like BeppoSAX or Suzaku, which can cover an extended energy range, are used to observe different celestial sources. These celestial sources may have distinct emission mechanisms that might be localized in varying regions of the electromagnetic spectrum. Therefore satellites like BeppoSAX or Suzaku, that we have used in this work to analyse data from a source, become of primary importance in order to comprehend these features in a better way. As the source of our study is a variable source, timing analysis becomes very important. This is done by the use of MAXI and ASM detectors (see further explanation in this chapter).

4.1 BeppoSAX

The Satellite per Astronomia X (SAX) was at first called SAX and the name was later changed to BeppoSAX after its launch in honour of Giuseppe Occhialini (Beppo was his nickname) was an important and major project led by the Italian Space Agency (ASI) [59], with participation of the Netherlands [60]. Space and ground segments were contracted to Alenia Spazio and Telespazio respectively [61]. BeppoSAX was launched from Cape Canaveral on April 30 1996, the satellite orbited at 600 km high and at a 3.9 degree inclination [62]. It operated successfully for 6 years with an energy range from 0.1 to 300 keV, a relatively large effective area and imaging capabilities in the range of 0.1 to 10 keV. It opened new perspectives in the study of spectral shape and variability of several classes of objects.

The research was of high importance for the understanding of different mechanisms

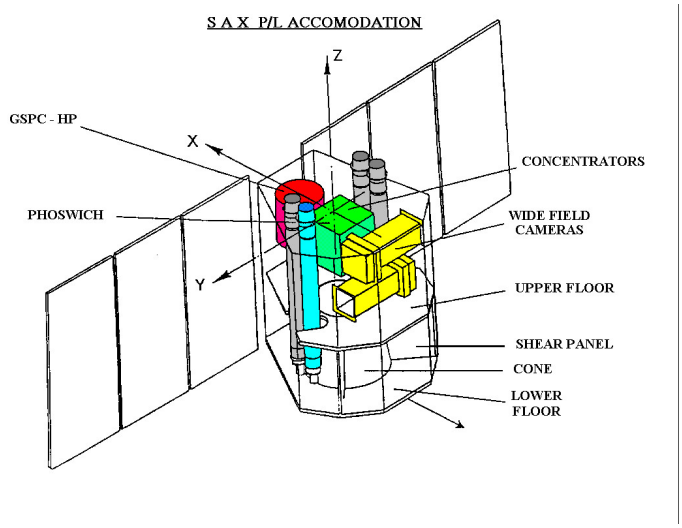

FIGURE 4.1: BeppoSAX instruments [63]

which produce spectral features localized in different regions of the electromagnetic spectrum. It also was able to locate bright Gamma Ray Bursts with unprecedented accuracy. Newer Satellites have used similar approaches inspired by this satellite rewarded by excellent results.

4.1.1 The Instruments

Four co-aligned instruments were installed on BeppoSAX, allowing for the broad energy range.
The wide band capability is provided by a set of instruments co-aligned with the Z axis of the Satellite. Narrow Field Instruments (NFI):

- The LECS (Low Energy Concentrator Spectrometer) is an imaging detector with an energy range of 0.1-10 keV. It has a thin window position sensitive gas scintillation proportional counter at its focal plane. It has an effective area of 22 cm^2 @ 0.28 keV, a field of view (FOV) of $37'$ diameter and an angular resolution of $9.7'$ FWHM @ 0.28 keV [64].

- The MECS (Medium Energy Concentrator Spectrometer) is an imaging telescope composed by a set of three identical incidence telescopes with double cone geometry (Critterio et al 1985, Conti et al 1994) with a average energy range of 1.3-10 keV, with position sensitive gas scintillation proportional counter at their focal plane. It

has an effective area of 150 cm^2 @ 0.28 keV, a field of view (FOV) of $56'$ diameter and an angular resolution for 50% total signal radius $75''$ FWHM @ 6 keV [65].

- The HPGSPC (High Pressure Gas Scintillation Proportional Counter). It has an energy range of 4-120 keV. It has an effective area of 240 cm^2 @ 30 keV [66].
- The PDS (Phoswich Detector System) has an energy range of 15-300 keV (Frontera et al. 1996). The lateral shields of the PDS are used as gamma-ray burst monitor in the range of 60-600 keV. It has an effective area of 600 cm^2 FWHM @ 80 keV [67].
- There are two coded mask proportional counters (Wide Field Cameras, WFC) situated perpendicular to the axis of the NFI and pointed in opposite directions It provides access to large regions of the sky in the range of 2-30 keV. Each WFC has a field of view of $20^{o}x20^{o}$ (FWHM) with a resolution of $5'$ [68].

4.2 Suzaku

The Suzaku Satellite (ASTRO-E2) is a X-Ray mission.
Launched on the year 2000, right after 42 seconds of its launch it suffered a major problem which made it fail its mission. Suzaku reused the ASTRO-E mission and it is considered as a step forward from the ASCA X-ray Satellite [69]. It is already the fifth mission accomplished by the Japanese X-Ray Satellites. The development of the Suzaku Satellite was done by a collaboration with US institutions, including NASA and the Japanese Institute of Space and Astronautical Science (hereafter ISAS). This institute belongs to the Japan Aerospace Exploration Agency, (hereafter JAXA) [70].
The Suzaku Observatory, was launched on July 10 2005 on a M-V-6 rocket. It was renamed Suzaku, the mythical Vermilion birth of the South, when the launch was considered a success.
Suzaku Observatory design makes it capable of performing observations in a wide energy range, from 0.2 up to 700 keV.
Suzaku has three major instruments:

- The X-Ray Imaging Spectrometer (XIS) is a detector arranged by 4 units, carrying each one a CCD camera with an energy range of 0.1-15 keV. Each one of them is combined with a single X-Ray Telescope (XRT). The CCD chips were provided by the Massachusetts Institute of Technology (MIT) providing a 1024x1024 pixels and covering a field of view of $18''$ region. The four units are divided in one unit back illuminated and the other three front illuminated. XIS 2 is a back illuminated CCD, whereas XIS 0, XIS 1 and XIS 3 are front illuminated [72].

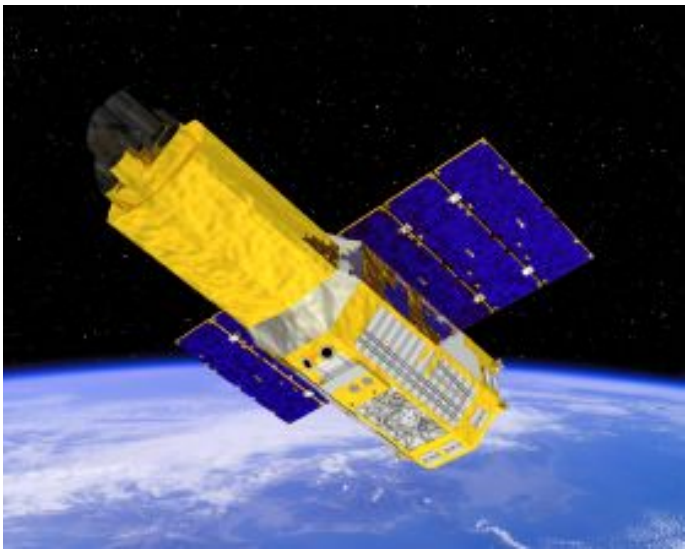

FIGURE 4.2: Suzaku Satellite [71]

- With an energy band of 10-700 keV, the Hard X-ray Detector (HXD) is another Suzaku detector. The HXD uses a combination of detectors to measure X-rays from a source in the sky. One type of detector (made of a crystal called BGO) is used as a vertical shield, forming a series of "wells". It is formed by the combination of silicon PIN diodes for energy bands lower than 50 keV and the GSO phoswich counters for photons above 50 keV [73].

- The X-Ray Spectrometer (XRS) consists of an array of X-ray micro calorimeters. The X-ray micro calorimeter consists of a 6 x 6 array of silicon detectors. It has been developed together by NASA/GSFC, Nagoya University, Tokyo metropolitan University and ISAS/JAXA. It has a moderate imaging capability and provides a large collecting efficiency. XRS can determine the energy of an X-ray to 0.1% [74].

The Suzaku Observatory is placed in orbit at an average altitude of 500km with a peak of 568 km. It follows an almost circular orbit at an inclination of 31.9^{o}. It has an orbital period of 96 minutes.
After the successful launch of Suzaku on July 10, 2005, the X-ray Spectrometer (XRS) was activated and performed to specifications for almost three weeks. Unfortunately, starting on July 29, the XRS experienced the first of a series of events associated with helium gas entering the vacuum space. On August 8 there were two such events, the second of which overwhelmed the dewar vacuum, resulting in the liquid helium boiling off and venting to space. Without the helium cryogenic, the XRS instrument can no longer provide the planned science. An investigation was being formed to understand the cause of this loss and to make recommendations for future missions [75].
On November 9 2006, one of the X-ray CCD cameras (XIS2), became suddenly unusable.

The attempts to recover XIS2 were unsuccessful [76]. The most likeable explanation for the failure comes from the impact of a micrometeoroid as seen already in XMM-Newton or in Swift.

4.3 MAXI

The Monitor of All-sky X-ray Image (hereafter MAXI), is an instrument for observing X-rays mounted on the exterior of the International Space Station Kibo module. It has been developed by JAXA and it is the first astronomical mission carried on the ISS to monitor all-sky X-ray images. It was launched in the Endeavour space shuttle on June 2009 and began observing and releasing light curves and energy spectra on August 2009. MAXI consists of X-ray slit cameras with high sensitivity. The ISS rotates around the Earth once every 96 minutes, meanwhile MAXI's two semicircular fields of view will scan the whole sky and monitors X-ray objects over an energy range of 0.5-30 keV [77].

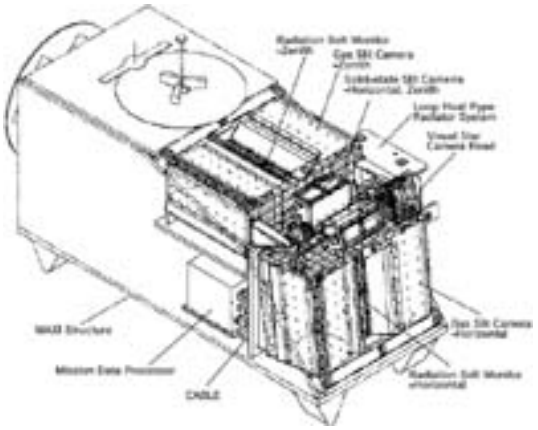

FIGURE 4.3: MAXI instrument [78]

It provides an average observation of 1000 X-ray sources per day, detecting transient phenomena, X-ray binaries, Gamma Ray Bursts, Active Galactic Nuclei and keeping the latest X-ray catalogue updated. Its detection sensitivity is about 20 mCrab for one orbit and 2-3 mCrab for one day.
MAXI carries two types of slit cameras:

- The Gas Slit Camera (GSC) is a slit camera with a Xe-filled proportional counter with 12 cameras, a large detection area in the 2-30 keV energy range, a sensitivity of 2 mCrab/week and an energy resolution of 15.7% at 8.0 keV [79].

- The Solid-state Slit Camera (SSC) is composed by 16 chips x 2 cameras CCD covering the 0.5 to 10 keV energy band, a sensitivity of 5 mCrab/week, and an energy resolution of 150 eV at 5.9 keV [79].

4.4 All Sky Monitor

The All Sky Monitor (hereafter ASM) is one of the instruments on board the RXTE satellite.
RXTE (Bruno B. Rossi X-Ray Timing Explorer) satellite, takes measurements and analyses the timely variation of X-ray emission. Launched on December 1995, it lasted until January 2012, staying operative longer than expected and being a widely extended mission.
ASM consists of three wide-angle cameras equipped with Xenon proportional counters. Manufactured by the MIT, it observes the long term behaviour of bright targets.
Properties:

- It has an energy range of 2 - 10 keV.
- It covers 80% of the sky every 90 minutes.
- Its collecting area is of 90 cm^2.
- It has a sensitivity of 30 mCrab.
- It has a field of view of 6×90^{o} [80].

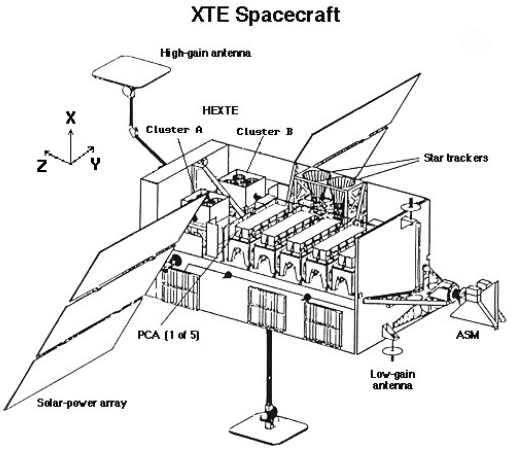

FIGURE 4.4: ASM on board RXTE observatory [81]

Chapter 5

4U 1916-053

5.1 4U 1916-053

4U 1916-053 is a X-ray binary located in the vicinity of the constellation of Aquila, close to the galactic center. Its latest estimated distance is of 8.9 kpc [82] [83]. The source was observed for the first time by the UHURU observatory in 1972 and it was originally named 2U 1912-05. This source was confirmed at a later time by the Ariel V satellite [84].

From the thermal flash model, the compact object of this system was confirmed as a neutron star. The recurrent X-Ray dips of 4U 1916-053 were discovered independently [85] with Einstein and OSO-8 observation, as well as in a later time by the EXOSAT observatory. [86].

4U 1916-053 consists of a neutron star as the compact object and a fully-degenerate or semi-degenerate helium white dwarf as the optical companion, therefore it is considered a LMXB [87]. From the timing and spectral behavior the source is believed to be a X-ray burster and dipping source with the shortest orbital period of all the dipping sources (50 min). The orbital period has been stable for more than 17 years [85]. 4U 1916-053 is an atoll source. An atoll source is believed to be a X-ray binary system which has a low magnetic filed neutron star and which shows type 1A bursts [88].

4U 1916-053 is believed to be at an estimated inclination angle of $\sim 60^{o} - 80^{o}$ [82] due to the periodic dips shown in its light curve. A highly coherent oscillation during a type I X-Ray burst indicates a fast spinning oscillation of the neutron star with a 3.7 millisecond period [89]. Moreover, QPOs are observed in the system, with frequencies from $\sim$ 0.2 to 1300 Hz [90].

4U 1916-053 shows spectral hardening during dipping, this feature although expected, it is not present in all observed dipping sources so far. From previous theoretical works, it

is expected to have a two blackbody component coming from two emission regions: The temperature in the boundary layer and the accretion disc [91]. Through the spectrum

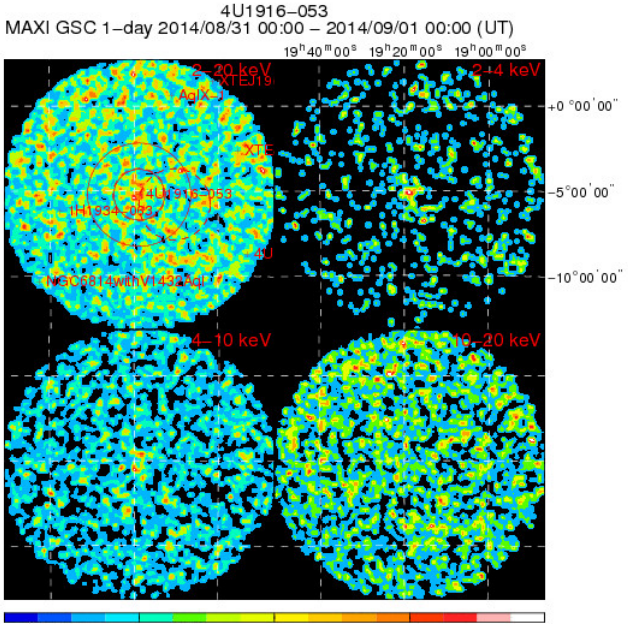

FIGURE 5.1: 4U 1916-053 from MAXI observation [92]

fitting, it is believed that 4U 1916-053 is an ADC source. By considering the column density variation with intensity, it has been suggested that the emission region of the disc-blackbody is much smaller than the power-law emission region [93].
Emission and absorption lines, specially of Fe XXV and Fe XXIV were also detected in this source. In our work, absorption lines were observed only during the persistent state absorption features are caused by highly ionized ions (iron or other metals), the lack of observed lines during the dip state implies that the bulge is less ionized [94].
The purpose of this thesis is the study of the spectral and timing behaviour of the source during both dip and persistent emissions with special emphasis on the spectroscopy study of emission and absorption features from the source. Furthermore we are interested in observing iron lines from the source. Indeed, as iron is the most abundant of the heavy elements, it is the easiest to observe and characterize.

5.2 Data

Two observations of the source were made with the BeppoSAX observatory: on 1997 April 27 (ObsID 2010600100) and on 2001 October 01 (ObsID 2137300200), with time exposures of 87 ks and 98 ks respectively. In the first observation, all the detectors were in use, but during the second observation, the HP detector was not in use and MECS1

was no longer operative. A burst was detected in the second observation.
On 2006 November 8th, the Suzaku observatory observed the source for 78 ks. Both the imaging and the non-imaging detectors were in use during the observation.
The data reduction in both observation types have been done with the software package offered by NASA, the High Energy Astrophysics software (hereafter HEAsoft), which also made the corresponding light curves and spectra needed for the study presented here [95].

5.3 Timing Analysis

5.3.1 Light-curves

BeppoSAX data was reduced using the standard software *xselect*. From this package we obtained the light curves for the instruments, LECS, MECS. The *hpproducts* package was specially used for data reduction and data products for the HP instrument obtaining spectra and light curves, as well as *pdproducts* for data reduction and data prducts for PDS instrument.

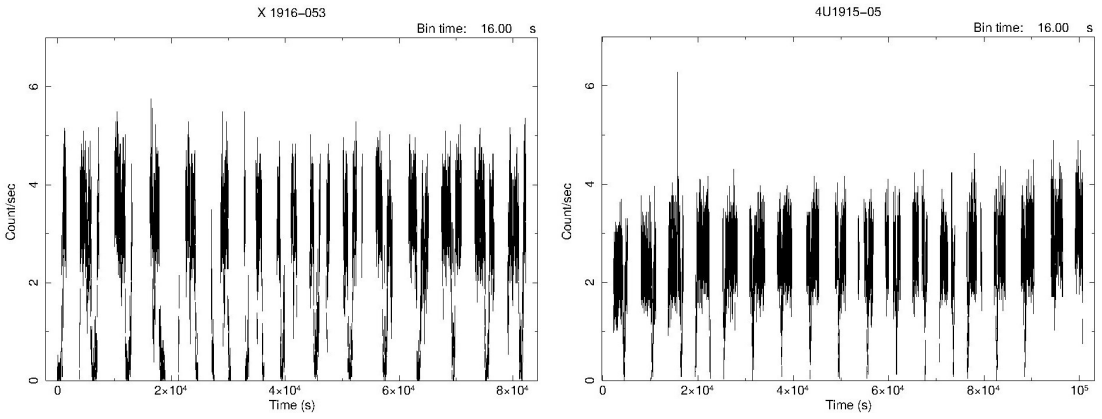

(A) MECS lc first observation (B) MECS lc second observation

FIGURE 5.2: MECS light curves in the 0.1-10 keV

The 5.2a figure is the light curve of the first observation done with BeppoSAX with the MECS instrument and the figure 5.2b corresponds to the second observation done with the same instrument. The MECS have an energy range of 0.1-10 keV. As previously mentionned, dips are periodic obscuration of the X-ray emitting region caused by material streamed into the accretion disc when it passes through the line of sight. It is expected at this energy range as it can be observed in both figures (see Figs. 5.2a and 5.2b). In both cases the dip regions are almost 100% deep.
Figures 5.3a and 5.3b corresponds to the same BeppoSAX observations done with the

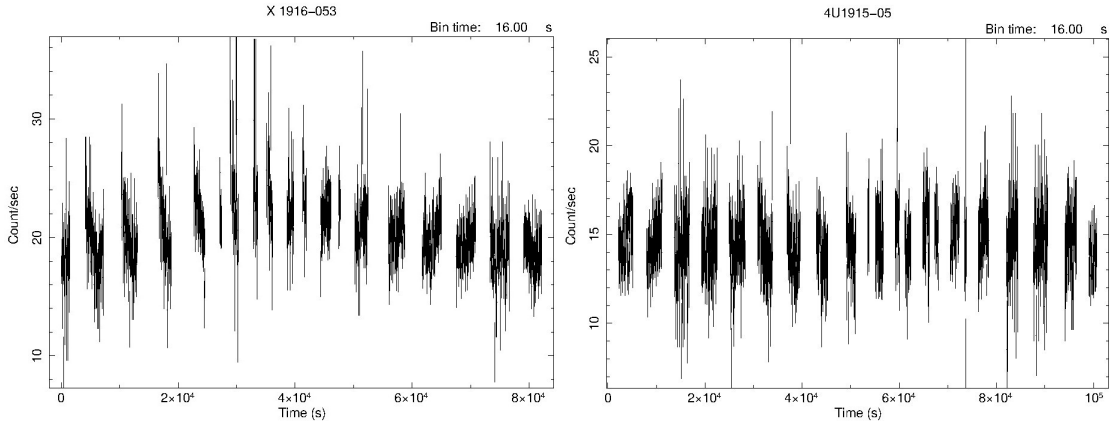

(A) PDS light curve light curve 1st observation (B) PDS light curve 2nd observation

FIGURE 5.3: PDS light curves in the 20-200 keV range

PDS instrument, which works in the 20-200 keV energy range. In this case, dips are mostly not present.

By comparison of the light curves from MECS and PDS, it can be established that dips are not a geometrical feature of the system. It is believed that in this case, the dip is produced by a structure located in the outer region of the disc and more specifically the impact region of the accretion flow from the companion star [96].

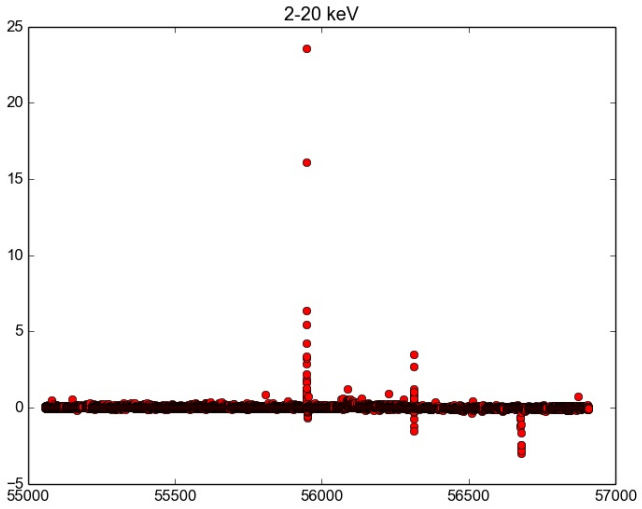

FIGURE 5.4: MAXI light curve in the 2 -20 keV with an X-ray burst

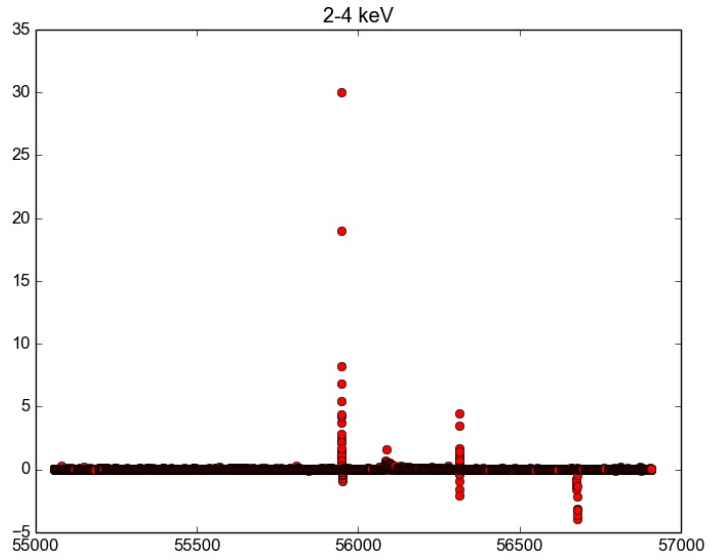

FIGURE 5.5: MAXI light curve in the 2-4 keV energy range

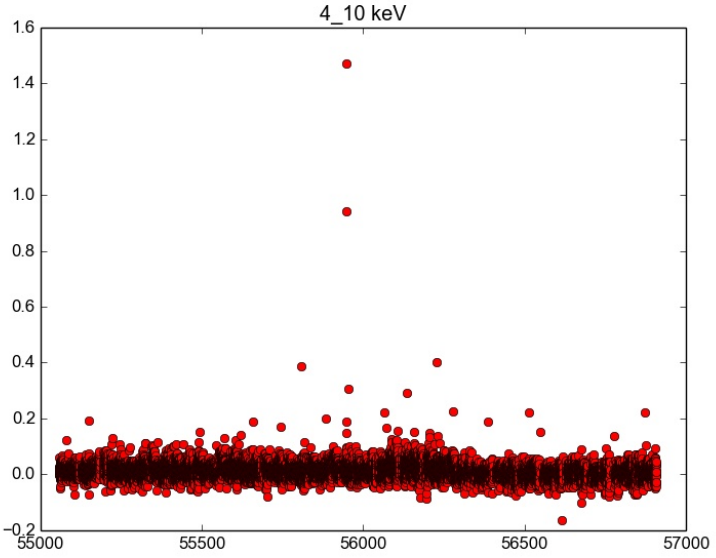

FIGURE 5.6: MAXI light curve in the 4-10 keV energy range

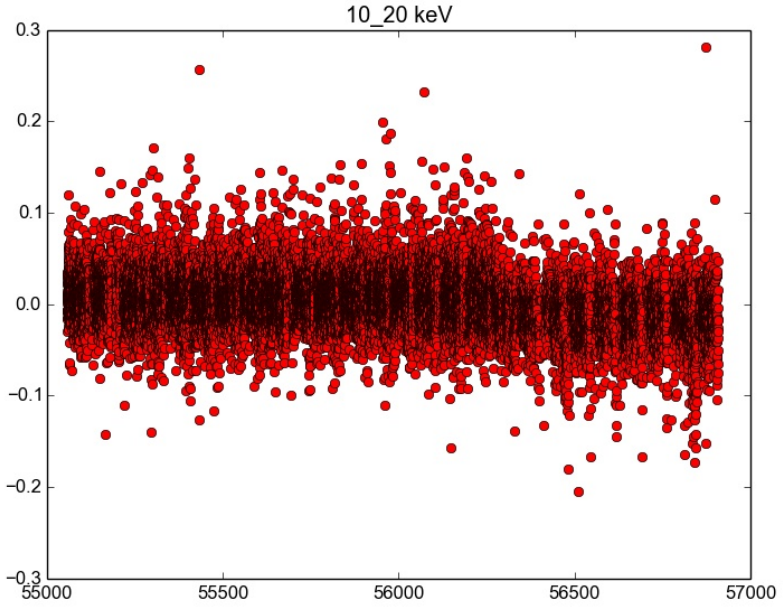

FIGURE 5.7: MAXI light curve in the 10-20 keV energy range

The light curve in the figure 5.4 represents the time evolution of the source in the 2 - 20 keV energy range,observed by MAXI [97]. In figure 5.5 the light curve is in the 2 - 4 keV energy range. A possible burst is observed. In figure 5.6 the light curve is in the 4 - 10 keV energy range and in figure 5.7 the light curve is in the 10 - 20 keV energy range. All of these light curves together represent the state of the source in four different energy bands. In these light curves, dips are not clearly identifiable because the use of MAXI light curves was more on the interest for creating a color color diagram (see Fig. 5.13) in order to see the variability of the system over a large period of time, opposing the short time provided by BeppoSAX and Suzaku.

The data from these light curves was downloaded from the MAXI webpage and the products were obtained with a python script [98], using numpy package specifically.

This research has therefore made use of the MAXI data provided by RIKEN, JAXA and the MAXI team [99].

Suzaku data reduction and data products were performed following the standard procedure [100]. Attitude correction, telemetry filtering of events, barycentric correction and binary orbital correction using IDL [101] was done following the standard procedure.

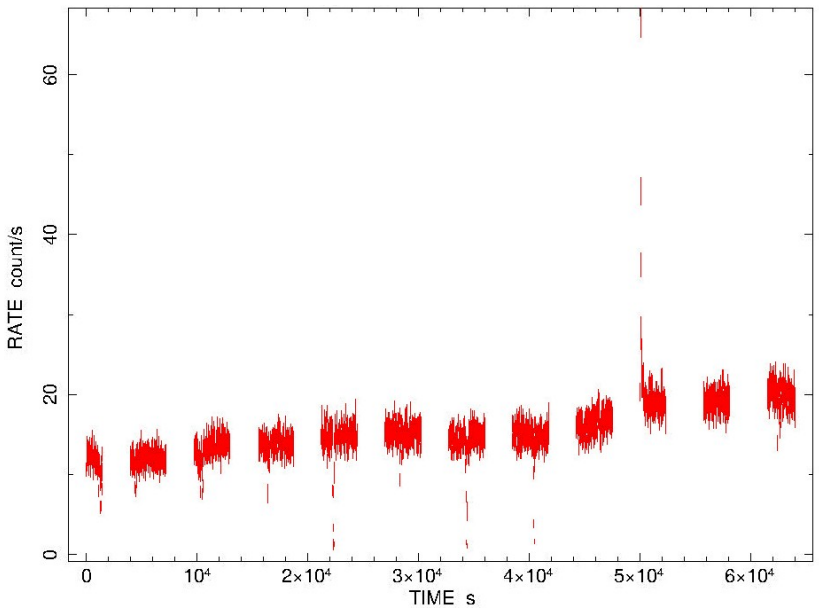

FIGURE 5.8: XIS light curve in the 0.1-15 keV energy range. X-ray burst present

The figure 5.8 corresponds to the Suzaku observation corresponding to XIS detector at an energy range of 0.1-15 keV. At this energy range dips are present. In this case, dips are narrower and not all of them are as deep as in the BeppoSAX observations. As dips are not depending on the geometry of the system, changes over time in the dip behaviour are expected to happen. A X-ray burst is present during the observation.

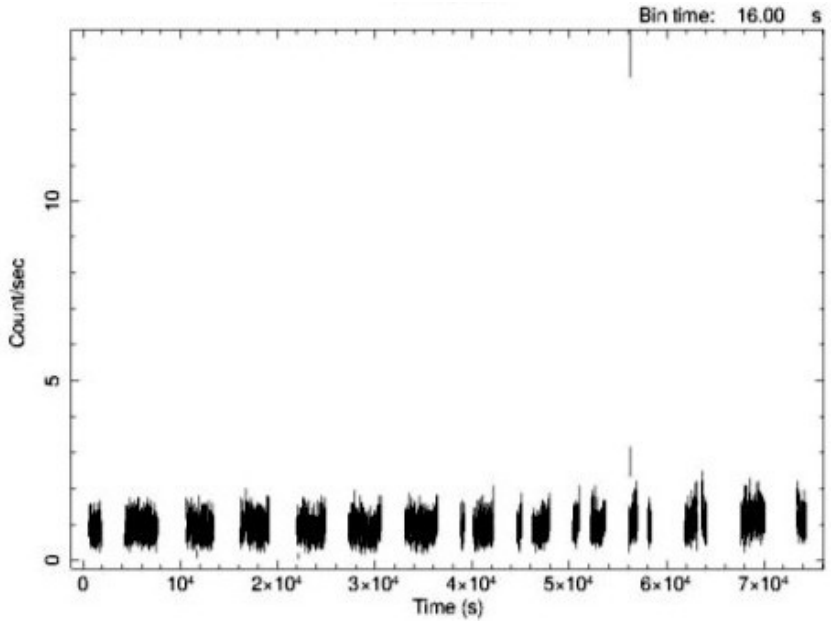

FIGURE 5.9: PIN light curve in the 12-50 keV energy range. X-ray burst radiation

In figure 5.9 we observe the light curve with the PIN detector in an energy range of 12-50 keV. In this case and to reassure dip feature, no dips are observed in a higher energy range.

From the study of the light curves with BeppoSAX, Suzaku and MAXI we can conclude the following: Dips only occur at a specific energy range (1 - 10 keV). They are very deep, almost as deep as an eclipse and they are produced periodically. Moreover, from BeppoSAX and Suzaku light curves the change of dip shape over time can be observed. Furthermore, we can conclude (as it has been already suggested in previous studies [85]) that dips are not a geometrical feature but they might occur due to absorption in the bulge in the outer accretion disc where the flow of the companion impacts the outer disc. More dip characteristics will be studied in the next sections.

5.3.2 Color color and hardness intensity diagram

From the data reduced in the two BeppoSAX observations, we used the *xselect* software package to obtain the light curves in three different energy bands, 1-4.5, 4.5-7 and 7-10.5 keV.

A color color diagram using BeppoSAX data was made using the MECS detector and by using a soft color (4.5-7 / 1-4.5 keV) in the X axis and a hard color (7-10.5 / 4.5-7 keV) in the Y axis.

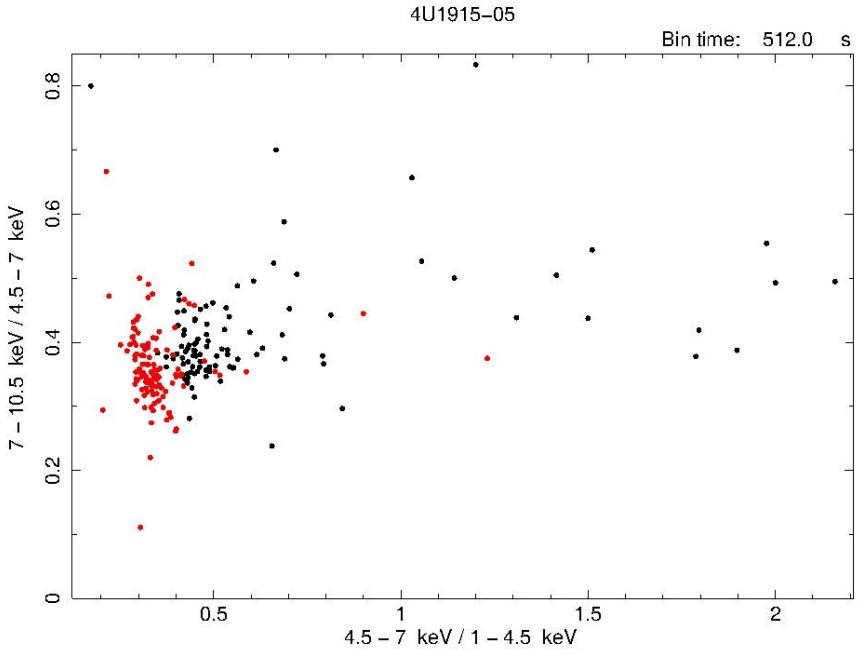

FIGURE 5.10: Color color diagram with BeppoSAX from two observations

We made a color color diagram combining both observations in order to compare them. We used the *lcurve* package to combine these light curves to form a color color diagram. Figure 5.10 shows a color color diagram combining the first observation (black) and the second observation (red). Due to the short observation time, the expected atoll shape is not observed specifically, but both cases do not exclude the banana shape as a possibility if longer measurements would have been available.

In both cases, the observations concentrates in one region, giving us the suggestion that both observations were in a similar state. In the harder state a clustering of several points can be pointed out. We will later discuss (using figure 5.11) that these correspond to the dips.

The color color diagram in the figure 5.11 corresponds to the substracted data omitting dips. The regions are easier to spot in this figure and show that both observations are in a similar state. From this figure we can suggest that the spectral hardening observed in figure 5.10 is due to the dipping behaviour.

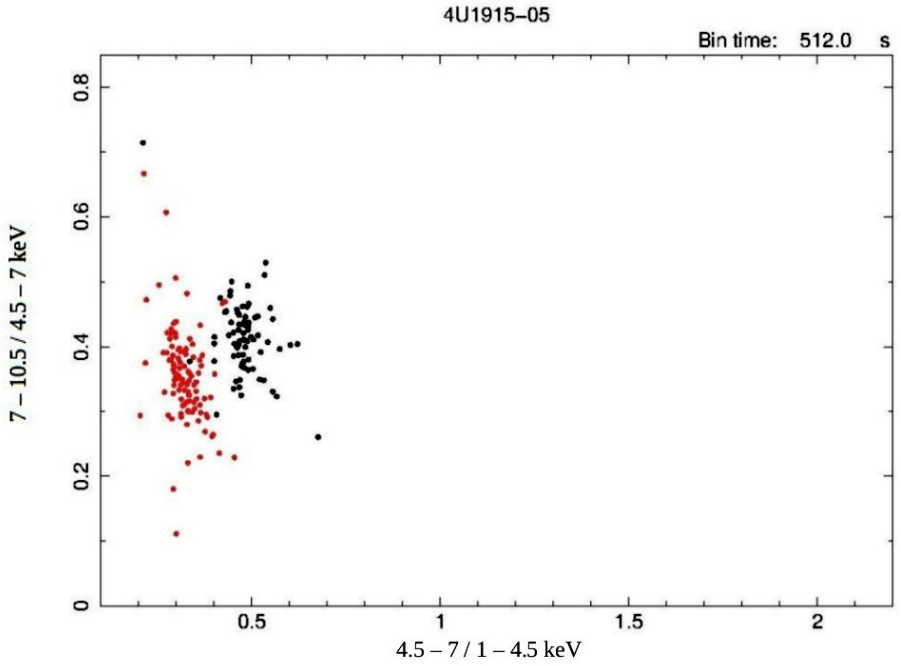

FIGURE 5.11: Color color diagram with BeppoSAX from two observations without dip

With RXTE/ASM we performed another color color diagram shown in the figure 5.12 . Thanks to its larger amount of time observation, we could obtain a color color diagram with a closer shape to an Atoll source. The ASM data was downloaded from the ASM light curves overview webpage [102] and the plot was done using a matlab program provided by Eva Laplace.

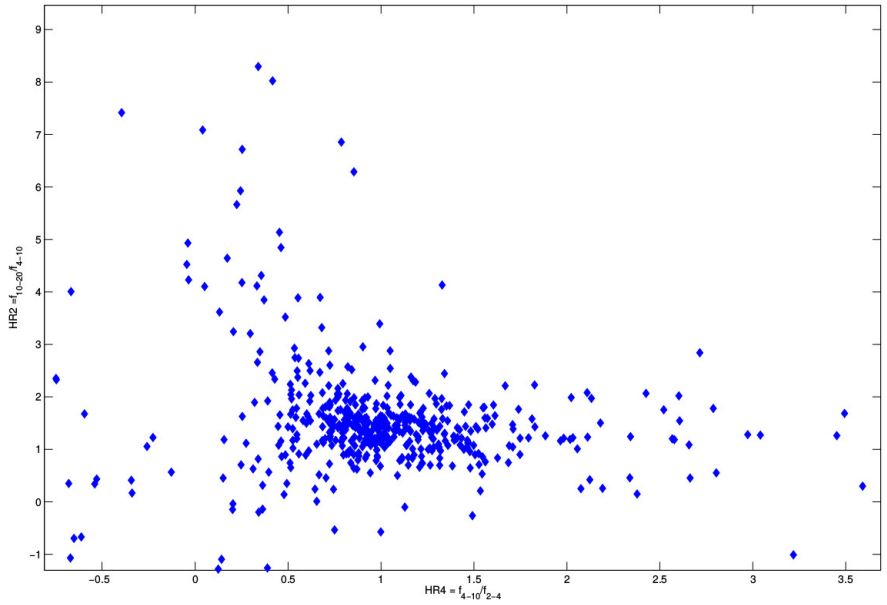

FIGURE 5.12: Color color diagram with ASM

Furthermore, we used orbital data from MAXI to create another color color diagram. In this case the energy ranges used were the ranges already provided by JAXA. 2-4, 4-10 and 10-20 keV (see figure 5.13). ASM provides a higher statistics than MAXI, therefore a less clear patterns are seen in the MAXI color color diagram.

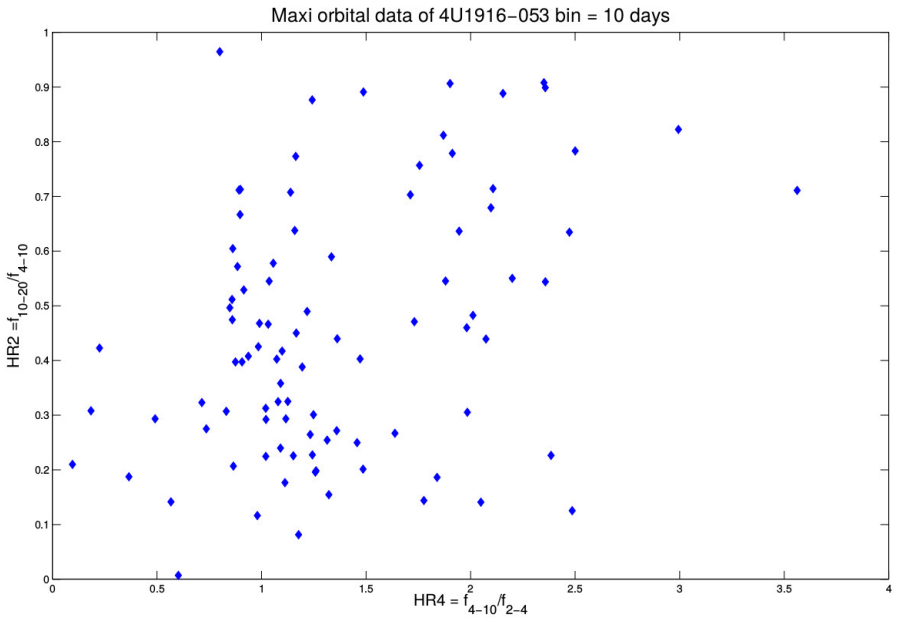

FIGURE 5.13: Color color diagram with MAXI

The variations in the color color diagram of the different instruments used can be explained by the differences in the energy band, which can lead to clustering of measurements of specific energies in one instrument that are not observed in the other one.
MAXI CCD is done without excluding dips, which can explain higher intensities due to the expected spectral hardening feature. However, from comparing the general shape of these color color diagrams, we can observe the "banana shape" and possible "islands", which leads to the confirmation that this source indeed shows the behaviour of an atoll source.
The next figure (see figure 5.14) is a hardness intensity diagram made from BeppoSAX observations. As in figure 5.10 spectral hardening can be observed as well. As it relies in the banana state, the shape of the plot remains quite constant over different intensities, which makes our assumption that both observations were in the banana state to be more reliable.

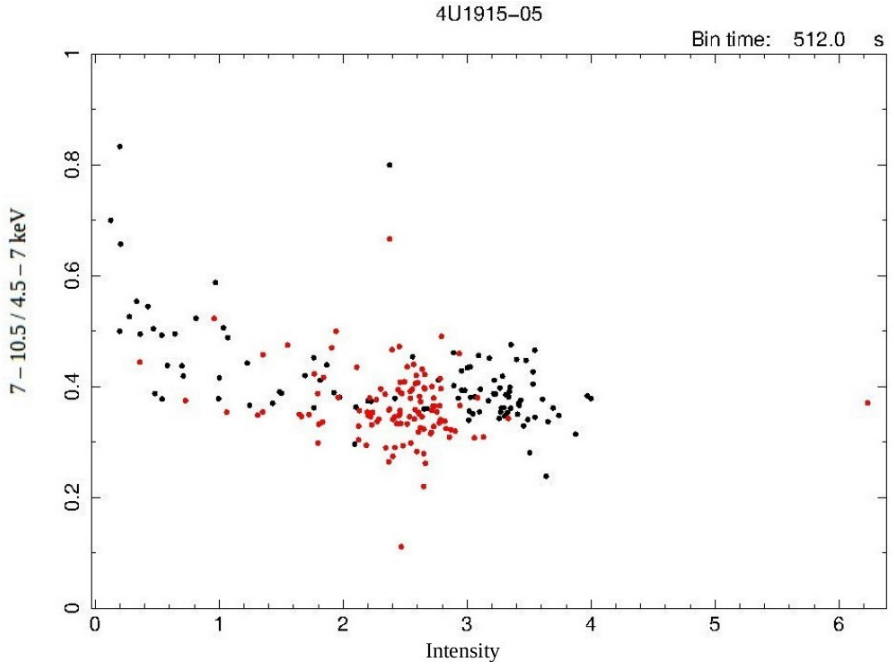

FIGURE 5.14: Hardness intensity diagram with BeppoSAX from two observations without dip

5.4 Spectral Analysis

For the data analysis performed on BeppoSAX and Suzaku data, two different versions of the HEAsoft software package were used: version 11.3 for BeppoSAX and version 12.8 for Suzaku, with specific use of the *xspec* software package. [103]
For a proper spectral analysis of the source, we needed to do the appropiate data reduction and make background substractions, corrections and calibrations.

5.4.1 Data reduction

The Suzaku data for XIS detectors is composed of three files: 2x2, 3x3 and 5x5. These modes are divided into the amount of pixels around the event center which are sent to the telemetry (25 for the 5x5, 9 pixels to the 3x3 and 4 pixel to the 2x2. Our data consisted of 3x3 and 5x5).
The Suzaku data reduction for XIS starts with recalibration and rescreening of the data using *aepipeline* command which encompass *xisgtigen, xistime, xiscoord, xisputpixelquality, xisgtigen, xistime, xiscoord, xisputpixelquality*, and *xispi*. We needed recalibration of the events creating a new attitude file performed by the *xiscoord* command, as well as barycentric correction with *aebarycen*. After obtaining image, region, spectra and background using *xselect*, XIS data 3x3 and 5x5 had to be combined, and eventually, XIS0, XIS2 and XIS3.

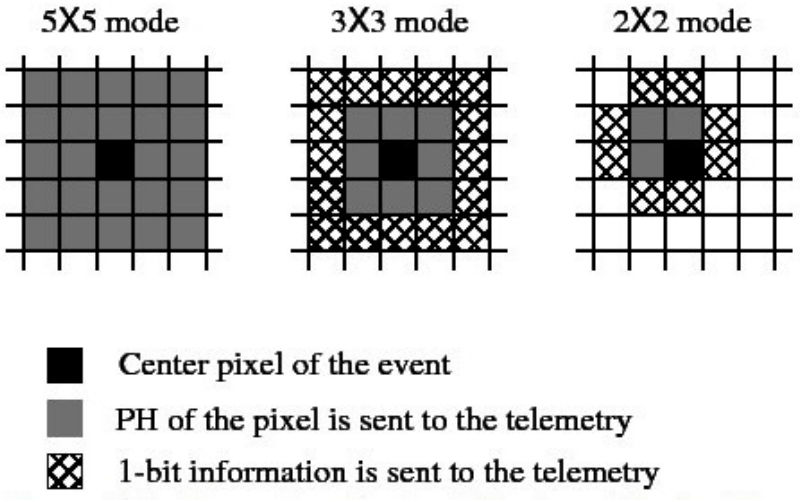

FIGURE 5.15: Data pattern for 5x5, 3x3, 2x2 [104]

For PIN data reduction *aepipeline* was used again. A common good time interval (GTI) was created with *mgtime*. Corrections like the South atlantic anomaly were performed by *xselect*, as well as dead time correction with *hxddtcor* and creation of spectra for the background.
For Suzaku data reduction the official guide [105] and different scripts provided by Slawomir Suchy were used [106].
BeppoSAX data reduction was done following the offical provided guide [107]. MECS instrument has three detectors that need to be merged together. We equalized MECS2 and MECS3 event files to the energy-pi scale of MECS1 using the *meevlin* command. We created a GTI file with *mgtime* and combined them together with *xselect*.
We used *xselect* to do the extraction in sky coordinates, light curve and spectra for LECS and MECS instruments.
Two other files were indispensable: The ancillary response file (hereafter ARF) and the redistribution matrix file (hereafter RMF). These files are required for both BeppoSAX and Suzaku data. Suzaku RMF and ARF files were produced by *xisrmfgen* and *xissimarfgen* respectively.
The RMF and ARF files are originally provided by the ASDC with precise use of the time of observation and the type of instrument for a correct use.

5.4.2 Fit models

Using the published literature about the source, we applied the current models to corroborate by these observations the behaviour of the source.

Non-Dip models	model description	command
(a)	Double bb	$wabs\,(bbody + bbody + cutoffpl)$
(b)	Comptonized	$edge{*}wabs\,(bbody + gaussian + gaussian + compTT)$
(c)	Simple bbody	$wabs\,(bbody + cutoffpl)$

TABLE 5.1: Model used in the persistent

1. (a) *The Double bb model* used in this case comes from the likelyhood of having two different blackbody components in the source. The Wien photon temperature kT_0 varies in a range of 0.4-2.5 keV (even if derived a similar blackbody temperatures).

These differences could be attributed to the existence of more than one blackbody component. At sufficiently high mass accretion rates, the boundary layer and the accretion disc are both radiating in the optically thick regime with 1 < kT < 2 keV. It is expected on theoretical grounds that the boundary layer has higher temperature than the accretion disc yielding two different blackbody temperatures in the X-Ray. [91].

2. (*b*) *the Comptonized model*. It is shown that the spectra comes from a mostly comptonized region. An edge is being observed at a low energy range. Two gaussian lines at 6.65 and 6.94 keV are also observed from spectroscopy.

3. (*c*) the *Simple bbody model* . It is a simple blackbody with a cutoff powerlaw. It was used to model the Suzaku data with XIS1 detector (BI) as an alternate solution because a second blackbody was not necessary.

The simple component models used are:

bbody	is a blackbody spectrum with distribution $A(E) = \frac{N_b 8.05251\ E^2 dE}{(k_B T)^4 \left(exp\left(\frac{E}{k_B T}\right) - 1\right)}$ $k_B T$ is the temperature in keV $N_b = \frac{L_{39}}{D_{10}^2}$ is the normalization L_{39} is the luminosity in units of 10^{39} erg s^{-1} D_{10}^2 is the distance to the source in units of 10 kpc
wabs	It is a photo-electric absorption using Wisconsincross-sections. $n_H = 0.26\ 10^{22}$ atms cm^{-2} $M(E) = exp(-n_H \sigma(E))$ $\sigma(E)$ is the photo-electric cross section n_H is th equivalent hydrogen column in 10^{22} atms cm^{-2}
pcfabs	A partial covering fraction absorption. $M(E) = f\ exp(-n_H \sigma(E)) + (1 - f)$ f is the covering fraction between 0 and 1. It is dimensionless.

cutoff powerlaw	A power law with high energy exponential rolloff. $A(E) = \mathrm{K}\ E^{-\alpha} exp\left(\frac{E}{-\beta}\right)$ α is the powerlaw photon index β e-folding energy of exponential rolloff in keV
gaussian	A simple gaussian line profile $A(E) = \mathrm{K}\ \frac{1}{\sigma\sqrt{2\pi}} exp\left(\frac{-(E-E_l)}{2\sigma^2}\right)$ E_l is the line energy in keV σ is the line width in keV. K is the total photons $cm^{-2}s^{-1}$ in the line.
Edge	The edge model is an absorption edge given by. $M(E) = \begin{cases} 1 & E \leq E_c \\ exp[-D\left(\frac{E}{E_c}\right)^{-3}] & E \geq E_c \end{cases}$ E_c is the threshold energy D is the absorption depth at the threshold
CompTT	This is an analytic model describing Comptonization of soft photons in a hot plasma, developed by L. Titarchuck. This replaces the Sunyaev-Titarchuck Comptonization model in the sense that the theory is extended to include relativistic effects. Δ is the Geometry switch. For ≤ 1, it is a disc geometry. > 1 is a sphere geometry.
diskline	A line emission from a relativistic accretion disc. $\left(1 - \sqrt{6/R}\right)/R^3$ accretion disc emissivity law is used
[108]	

TABLE 5.2: Xspec components for modeling data

Several models for the non-dip and dip were investigated in this work and are described in the tables 5.1 and 5.6.

5.4.3 Persistent spectra

The different spectra acquired from the data reduction, both from BeppoSAX and Suzaku were modeled with different components.

5.4.3.1 BeppoSAX persistent spectra

We fitted the BeppoSAX observations with the *Double bbody model* (see Table 5.1), excluding all dips. The data was fitted throughout the whole spectrum (see Fig. 5.16 and Fig. 5.17)

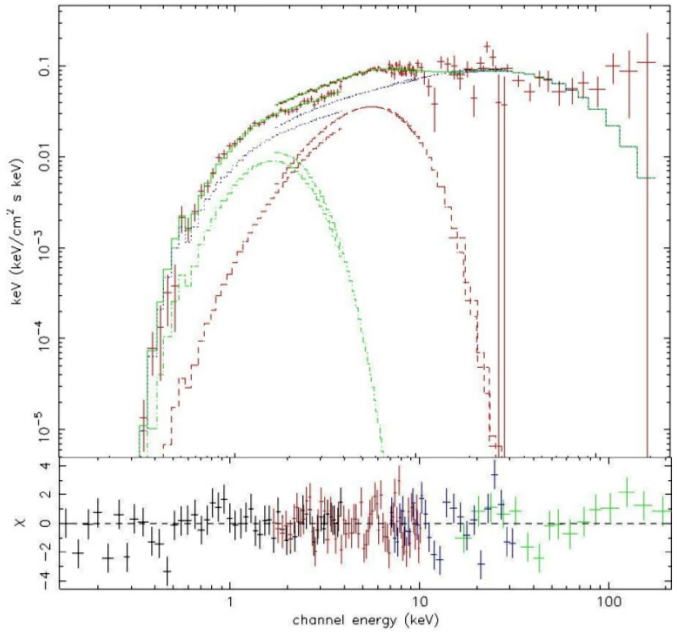

FIGURE 5.16: Unfolded energy spectrum extracted from non dip data of the 1st observation BeppoSAX with best fit and residuals using model Double bb

Figure 5.16 shows the unfolded energy spectrum extracted from non dip data of the first BeppoSAX observation with best fit and residuals with the *Double bb model*. Figure 5.17 shows the unfolded energy spectrum extracted from non dip data of the second BeppoSAX observation with best fit and residuals with the *Double bb model*.
From the timing analysis, it was established that both observations are in the "banana state", from where it can be assumed that they have a similar mass accretion rate $\dot{m}$ and therefore they should have a similar blackbody temperature [109].
The table 5.3 shows the fits obtained in figures 5.16 for the first observation and 5.17 using the *Double bb model*. Very similar temperatures obtained in the best fit for both blakcbodies, 1.45 and 1.42 keV for the first blackbody and 0.37 and 0.40 keV for the second blackbody corroborate that both observations are in the "banana state". The

first observation has a cut-off energy $E_{CO} = 41$ keV and the second observation has a $E_{CO} = 49$ keV. Below 10 keV, where photoelectric absorption is dominant, the spectral changes observed during dips can be simple modeled by progressive covering of the blackbody and cut-off power law components (see section 5.4.4) It can also be observed in both figures that the source is detected at energies ≥ 100 keV.

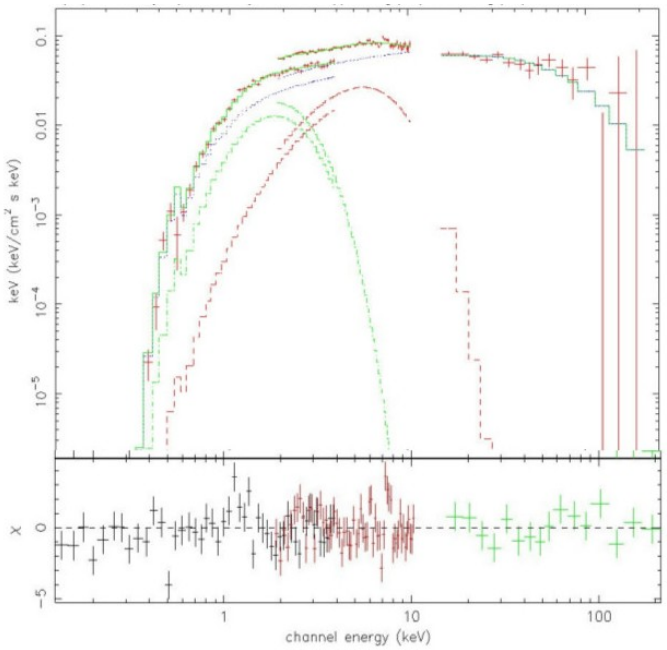

FIGURE 5.17: Unfolded energy spectrum extracted from non dip data of the 2nd observation BeppoSAX with best fit and residuals using model Double bb

	First observation	Second Observation
χ^2	1.50	1.50
$n_H\ (10^{22} cm^{-2})$	0.24 ± 0.05	0.32 ± 0.05
kT_{bb}	1.45 ± 0.06	1.42 ± 0.01
$norm_{\ bb}$	9 ± 2×10^{-4}	7 ± 2×10^{-4}
kT_{bb}	0.37 ± 0.03	0.40±0.02
$norm_{\ bb}$	4 ± 2×10^{-4}	6 ± 3×10^{-4}
Γ	1.3 ± 0.1	1.6 ± 0.2
E_{CO}	41 ± 9	49 ± 14
norm	2.0 ± 6×10^{-2}	3.1 ± 0.1×10^{-2}

TABLE 5.3: BeppoSAX non-dip Best fits Parameters

5.4.3.2 Suzaku persistent spectra

In the study of Suzaku spectra, due to differences in the XIS instrument, severeal approaches had to be taken into consideration. As already mentionned in the previous chapter (Sec. 4.2), the XIS instrument is composed by 4 detectors. Three of them are front illuminated and the fourth one is back illuminated. This difference is due to the position of the electronics inside the device. From this difference, the back-illuminated detector (hereafter BI) has a substantial improved sensitivity at energies below 2 keV. On the other side, the front-illuminated detectors (hereafter FI) have higher sensitivities than the BI in the high energy range.

For this Suzaku analysis, the study has to be done individually for FI and BI data combined with PIN. In the case of the FI detectors, XIS0, XIS2, XIS3, they were either combined together or plotted separatelly. The BI detector XIS1 was fitted alone with PIN.

We fitted the Suzaku observation with the *simple bbody model* (see Table 5.1) excluding all dips. The data was fitted throughout the whole spectrum.

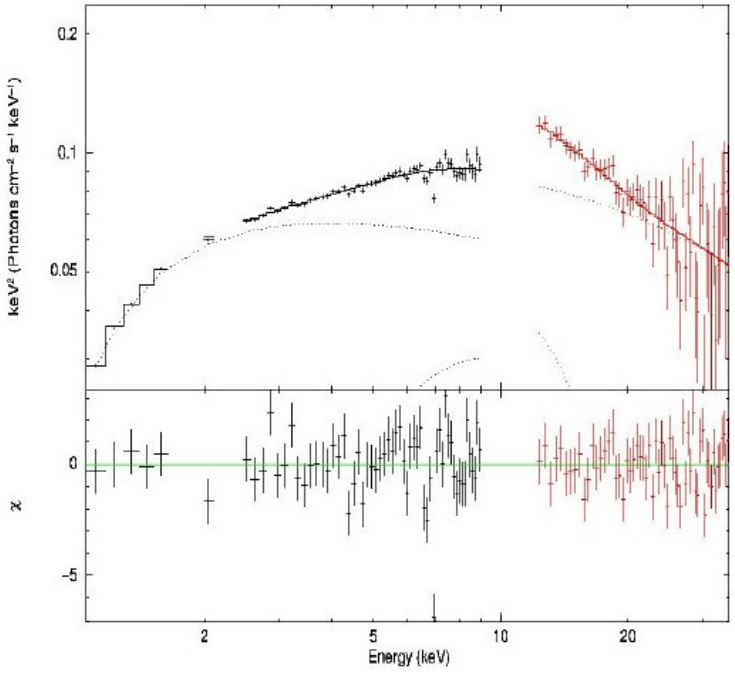

FIGURE 5.18: Unfolded energy spectrum extracted from non dip data of the XIS03+PIN Suzaku observation with best fit and residuals using model Simple bbody

Figure 5.18 shows the unfolded energy spectrum extracted from non dip data of the Suzaku observation with best fit and residuals with the *Simple bbody model*. From this model, we obtained a χ^2 of 1.64, which we could improve. It can be observed negative residuals at an energy range of 6.65 and 6.95 keV. We decided to leave this model because of the poor fits obtained for this observation and use the *comptonized model*.

We fitted the Suzaku observation with the *Comptonized model* (see Table 5.1), excluding all dip behavior (see Fig. 5.19).

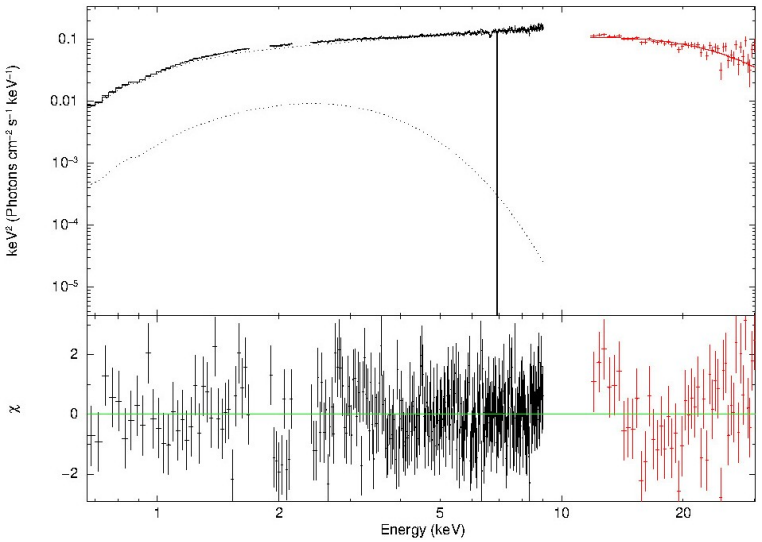

FIGURE 5.19: Unfolded energy spectrum extracted from non dip data of the XIS03+PIN Suzaku observation with best fit and residuals using model Comptonized

Figure 5.19 shows the unfolded energy spectrum extracted from non dip data of the Suzaku observation with best fit and residuals with the *Comptonized model* using XIS03 + PIN detectors. The spectrum is dominated by non thermal emission, mostly comptonized. Negative residuals were observed and modelled. We added two gaussians at 6.65 and at 6.95 keV, corresponding to Fe XXV and Fe XXVI Kα respectively, improving our fit and testing it using the command *ftest*. An edge was observed and modelled as well at 0.99 keV improving our fit, as was already seen in a observation of the same source done by XMM-Newton satellite [110].

In the figure 5.19 we used the *comptonized model* with the XIS 0 and XIS 3 detectors together with PIN and in the figure 5.20 we used the same model but adding XIS 2 to the fit increasing our statistics in the 1 - 10 keV energy range.

Differencies between both fits can be seen in the table 5.4.

The difference in the Edge observed at 0.88 keV with XIS03 and at 0.98 with XIS023 comes from the broad selection of the spectrum. In figure 5.19 the spectrum is modelled from 1 keV and in figure 5.20 is modelled from 0.6 keV leading to these differences.

Suzaku data carries two edges, a Si edge at 1.72-1.88 and a Au edge at 2.19-2.37 keV that needed to be ignored in our study for all XIS detectors.

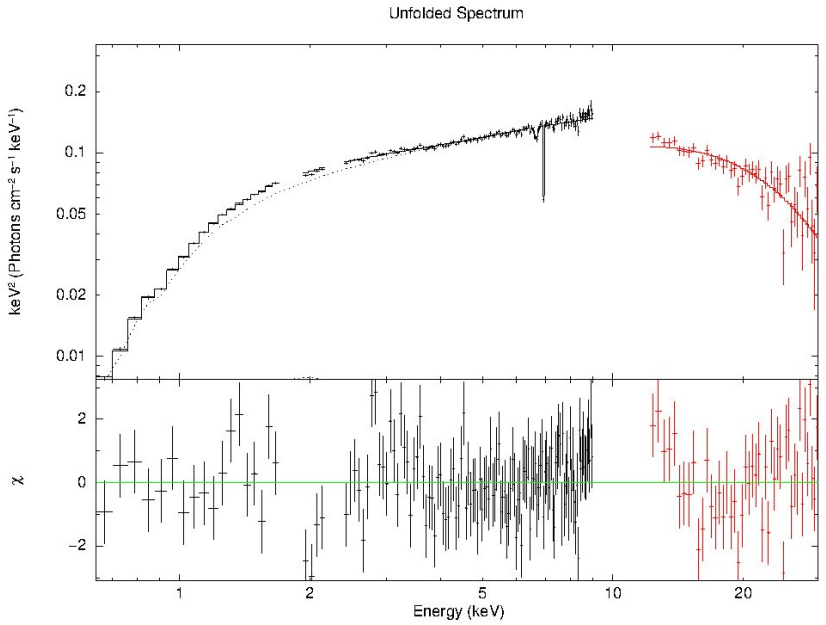

FIGURE 5.20: Unfolded energy spectrum extracted from non dip data of the XIS023+PIN Suzaku observation with best fit and residuals using model Simple bbody

	FI 03	FI 023
χ^2	1.41	1.41
$E_{edge}\,(keV)$	0.88 ± 0.02	0.98 ± 0.10
τ	0.06 ± 0.02	0.01 ± 0.01
$n_H\,(10^{22}cm^{-2})$	0.25 ± 0.03	0.32 ± 0.05
kT_{bb}	0.58 ± 0.03	0.43 ± 0.02
$norm_{\ bb}$	(2 ± 0.5)x·10^{-4}	(2 ± 0.3)x·10^{-4}
E_{line}	6.65 ± 0.02	6.65 ± 0.03
$\sigma\,(eV)$	0.04 ± 0.05	0.04 ± 0.02
EW(eV)	(5 ± 1)x·10^{-4}	(5 ± 1)x·10^{-4}
E_{line}	6.94 ± 0.01	6.94 ± 0.01
$\sigma\,(eV)$	(3 ± 1)x·10^{-6}	(4 ± 1)x·10^{-6}
EW(eV)	(9 ± 1)x·10^{-5}	(9 ± 1)x·10^{-5}
$\text{CompTT}_{\text{t0}}$	0.23 ± 0.02	8.63 ± 0.09
$\text{CompTT}_{\text{tk}}$	4.49 ± 0.10 ·10^{-2}	4.61 ± 0.11·10^{-2}
τ	5.68 ± 0.11	5.39 ± 0.10
$norm$	0.03 ± 0.01	0.06 ± 0.05

TABLE 5.4: Comptonized Suzaku Best fits Parameters

Table 5.4 shows the best fit obtained from using XIS03 with PIN and XIS023 with PIN. Iron lines in both cases were detected at the same energy range, proving the observation of the iron lines. The blackbody temperature differs between both cases, with 0.58 keV for the XIS03 and 0.43 keV for the XIS023. In this model the spectrum is mostly comptonized as shown in the table.

We fitted the Suzaku observation with the *simple bbody model* (see Table 5.1), excluding all dips with XIS 1 (BI) + PIN. The data was fitted throughout the whole spectrum (see Fig. 5.21).

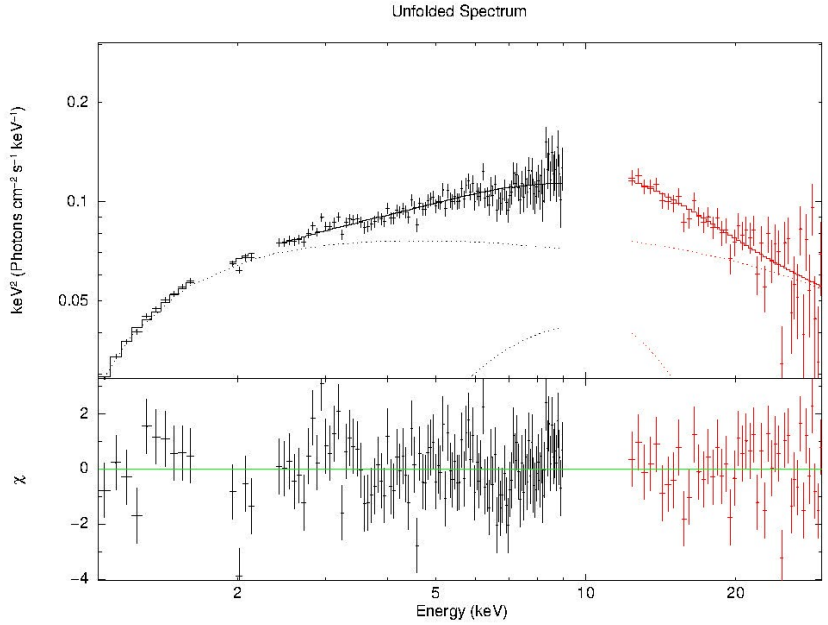

FIGURE 5.21: Unfolded energy spectrum extracted from non dip data of the XIS1+PIN Suzaku observation with best fit and residuals using model Simple bbody

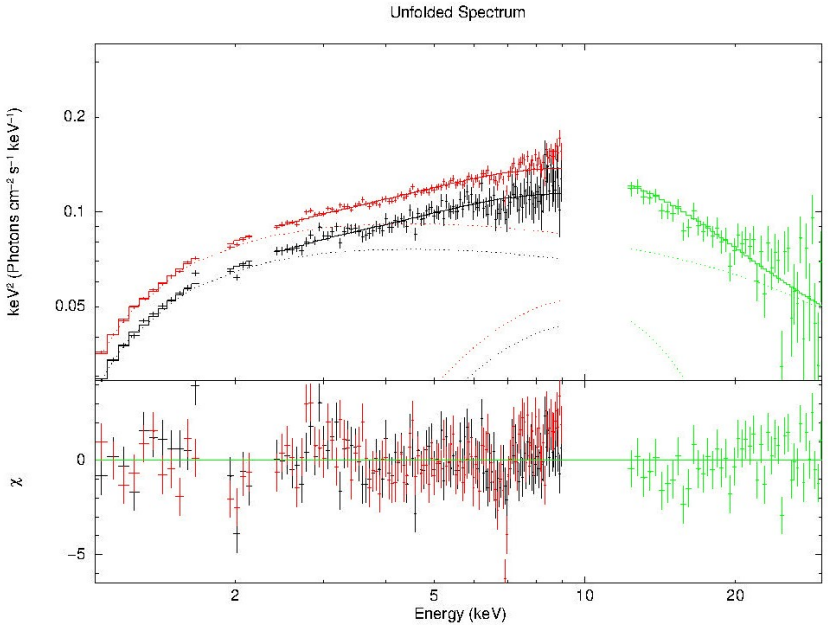

FIGURE 5.22: Unfolded energy spectrum extracted from non dip data of the XIS0123+PIN Suzaku observation with best fit and residuals using model Simple bbody

We fitted the Suzaku observation with the *simple bbody model* (see Table 5.1), excluding all dips with XIS 1 (BI) and XIS023 + PIN. The data was fitted throughout the whole spectrum (see Fig. 5.22).
Intercalibration constants were left free for XIS023 and for PIN, fixing XIS1 to 1. Negative residuals are observed at 6.5 - 6.9 keV energy range but we could not fit any line in this case. A poor fit χ^2 of 1.53 could be explained due to the differences of the front and back illuminated detectors fitted together.
Differencies are present depending on the use of FI and BI detectors, causing differences in the background level, resulting in completely different models in our fits. For comparison, in figure 5.22 using *the simple bbody model*, we fitted the FI and BI XIS detectors together.
The temperature of the blackbody obtained from the BI fit was 2.40 keV, with an energy cut off $E_{CO} = 41 \pm 9$ and gave us a χ^2 of 1.18 giving a good fit.

(*c*) model	BI	FI + BI
χ^2	1.18	1.53
$n_H\ (10^{22} cm^{-2})$	0.51 ± 0.03	$0.47 \pm 1.49{\cdot}10^{-2}$
kT_{bb}	2.40 ± 0.16	3.10 ± 0.20
$norm_{\ bb}$	$9 \pm 2{\cdot}10^{-4}$	$1.23 \pm 0.11{\cdot}10^{-3}$
Γ	1.3 ± 0.1	$1.84 \pm 3.88{\cdot}10^{-2}$
E_{CO}	41 ± 9	29.02 ± 5.84
norm	$2.0 \pm 6{\cdot}10^{-2}$	$7.73 \pm 0.15{\cdot}10^{-3}$

TABLE 5.5: Simple bbody Suzaku Best fit parameters

5.4.4 Dip spectra

4U 1916-053, as most dippers, shows spectral hardening during dipping. However, the spectral evolution is not consistent with a simple increase of photo-electric absorption by cool material, as an excess of photons is present at low energies. Two approaches have been proposed for modelling the spectral evolution during dips.

1. In the "absorbed plus unabsorbed" approach [111], the persistent model is used to fit the intensity selected dip spectra, but is divided into two parts. One part is allowed to be absorbed, whereas the other one is not. The spectral evolution during dipping is well accounted for by a large increase in the column density of the absorbed component, and a decrease of the normalization of the unabsorbed component.

2. In the progressive covering approach, the X-Ray emission originates from two components. The first one, generally modelled as a blackbody, is from a point-like region, such as the boundary layer around the compact object. The second

component, generally modelled as a power-law, comes from an extended region, such as an accretion disc's corona.

We chose the "partial covering" scenario for the scope of this thesis because in the "absorbed plus unabsorbed" model, a latter decrease of the normalization of the unabsorbed component has been attributed to effects of electron scattering in the absorber, but it cannot represent a decrease in brightness of the source, therefore there are some difficulties in finding a physical explanation for this decrease [96].
The dip modelling of the source is done in this thesis by using only the observed dips from the light curves in BeppoSAX and Suzaku.
From the BeppoSAX light curves, the complete dip has to be taken into account, because the statistics are not high enough.
In the case of Suzaku dips, two approaches are used. The dips in the Suzaku light curves are different from the ones of the BeppoSAX observation: not all the dips are very deep. The approach has been to compare all the possible dips with the ones that are the deepest and to see the difference in the covering component. Therefore two different time selections were made.

Dip models		
(a)	Partial covering	$(wabs * pcfabs * cutoffpl)$
(b)	Partial covering bbody	$(wabs\,(bbody) + wabs * pcfabs\,(cutoffpl))$
(c)	Partial covering diskline	$(wabs\,(bbody) + wabs * pcfabs\,(cutoffpl + diskline))$

TABLE 5.6: Models used during dips

In the table 5.6 the models we used are shown in detail. For Suzaku observation we used the *Partial covering model* whereas BeppoSAX observations were fitted with the *Partial covering bbody model* and *Partial covering diskline model*. The difference between the *Partial covering bbody model* and *Partial covering diskline model* lies on a possible diskline component added in one of the fits that will be discussed later.

5.4.4.1 Suzaku dip spectra

The dip spectrum of Suzaku is divided in various sections. As it can be seen in the light curve from XIS detector (see Fig. 5.8), the dips are very narrow and only a few of them are as deep as the ones observed on BeppoSAX (see Fig. 5.2b).
In figures 5.23, 5.24 and 5.25 all possible dips were taken into account and in all of these cases a *Partial covering model* was used to model the spectrum.

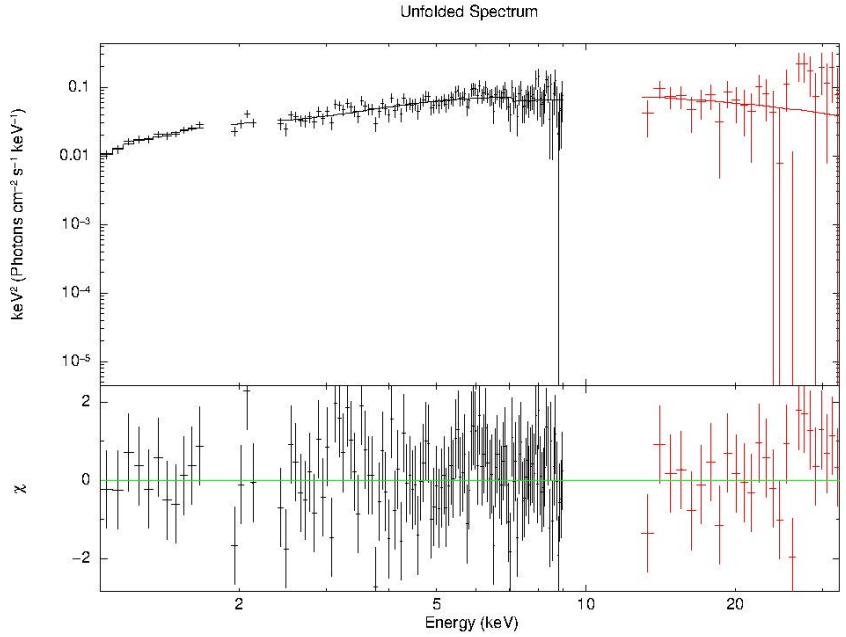

FIGURE 5.23: Unfolded energy spectrum extracted from dip data of the XIS03+PIN Suzaku observation with best fit and residuals using model Partial covering

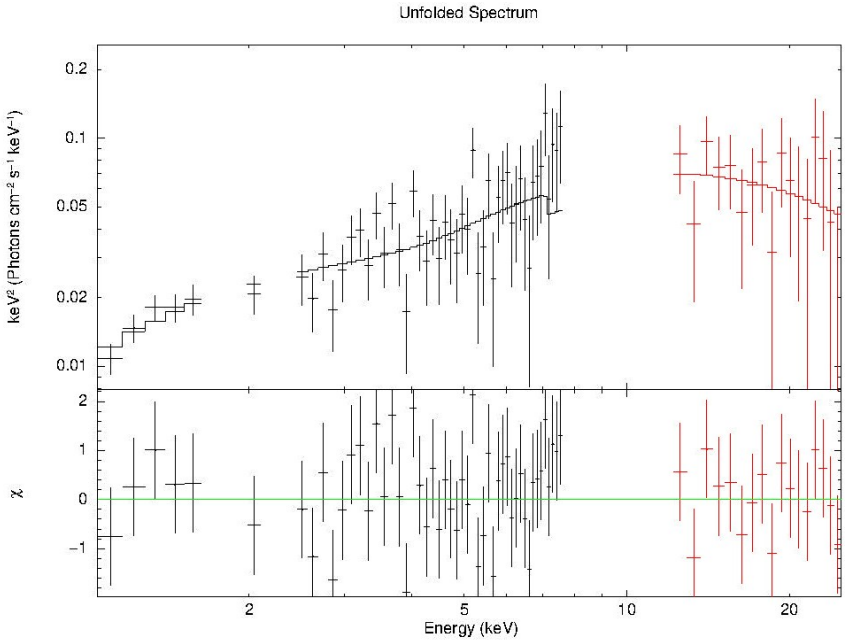

FIGURE 5.24: Unfolded energy spectrum extracted from dip data of the XIS1+PIN Suzaku observation with best fit and residuals using model Partial covering

A cut in the XIS instruments at 8 keV was done due to poor statistics in the higher energy range. As it can be compared from figure 5.23 and 5.24, there are better statistics for the FI instrument than for the BI. In table 5.7 we can see the fit results for Suzaku

	FI-03 dip	BI	FI-BI	3 Dip
χ^2	0.90	0.86	0.92	0.95
$n_H\ (10^{22} cm^{-2})$	0.68 ± 0.16	0.25 ± 0.27	0.59 ± 0.16	0.90 ± 0.25
$n_H\ (10^{22} cm^{-2})$	16.58 ± 3.65	44.75 ± 38.96	17.63 ± 4.46	46.21 ± 13.60
f	0.61 ± 0.10	0.53 ± 0.23	0.56 ± 0.10	0.74 ± 7.97·10^{-2}
Γ	2.02 ± 0.34	1.43 ± 0.50	1.91 ± 0.36	1.79 ± 0.45
E_{CO}	28.89 ± 21.44	13.37 ± 9.60	32.47 ± 47.70	10.92 ± 8.18
norm	0.11 ± 4.94·10^{-2}	4.20 ± 3.26·10^{-2}	8.75 ± 4.10·10^{-2}	0.14 ± 8.90·10^{-2}

TABLE 5.7: Partial covering Suzaku Best fit parameters

observation. In the FI case we only fitted XIS0 and XIS3 together. A higher covering was observed with the FI instrument than with the BI. In all cases a good fit was obtained, χ of 0.90 for the FI and 0.86 for the BI.

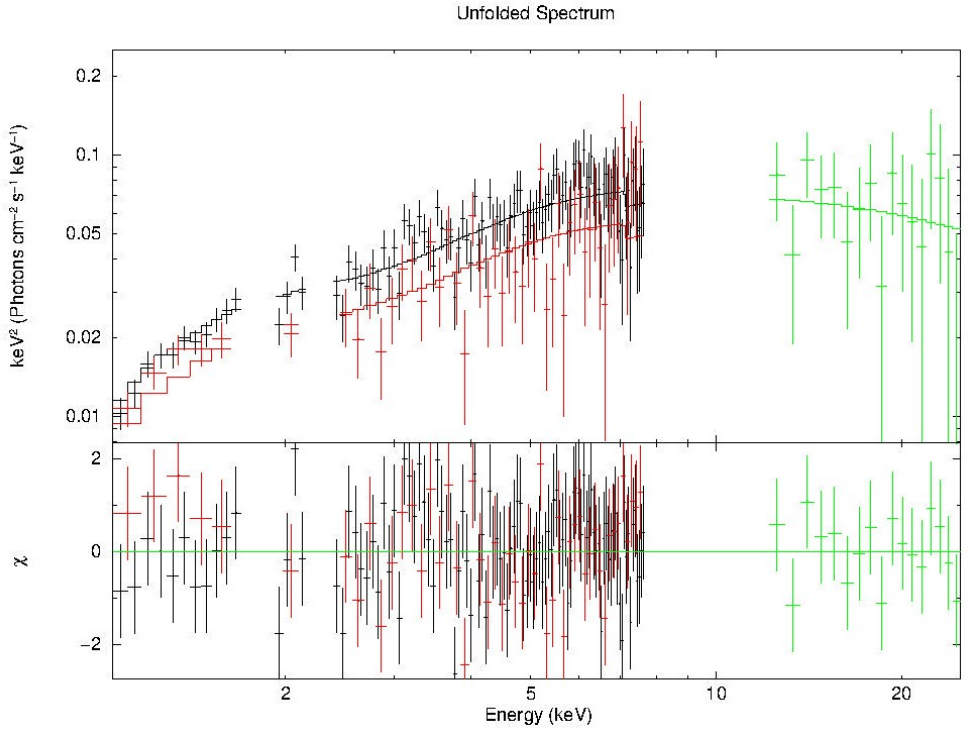

FIGURE 5.25: Unfolded energy spectrum extracted from dip data of the XIS 0123+PIN Suzaku observation with best fit and residuals using model Partial covering

In the figure 5.25 we observe the fit of both FI and BI together.

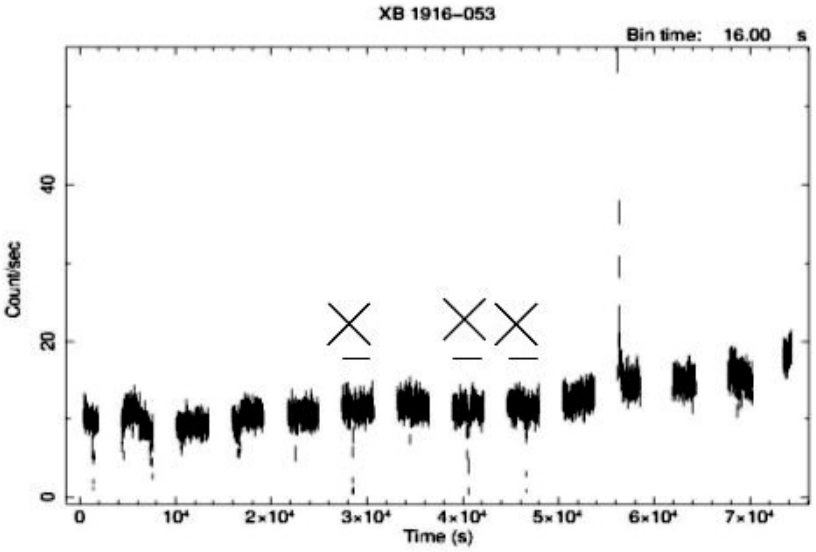

FIGURE 5.26: XIS light curve with 3 dips included

Three specific dips were chosen (see Fig. 5.26) for a study of the deep dips.

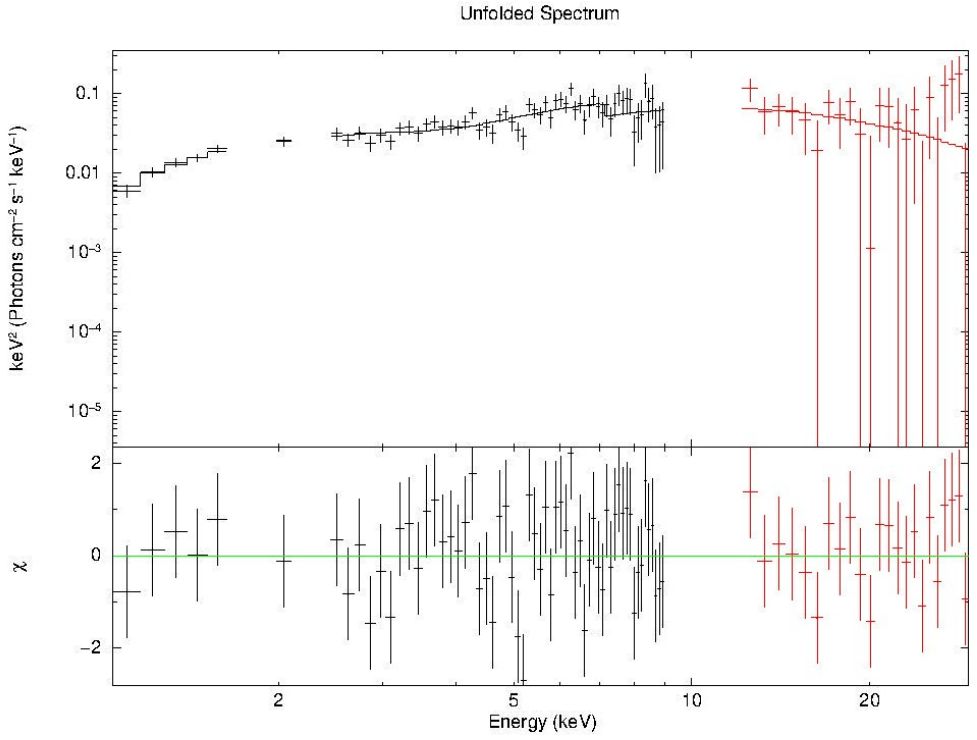

FIGURE 5.27: Unfolded energy spectrum extracted from dip data (see Fig. 5.26) of the XIS 03+PIN Suzaku observation with best fit and residuals using model Simple bbody

Figure 5.27 corresponds to the spectrum in the three corresponding dips. From the table 5.7 we have a higher covering fraction as expected, obtainig a good fit with $\chi = 0.95$. Only the FI instrument were used for this approach.

There were less amount of statistics in this approach. Table 5.7 shows higher value for the column density in this approach compared to the other Suzaku spectra with $n_H\left(10^{22}cm^{-2}\right) = 46.21 \pm 13.60$ but with a high uncertainty, comparable to the spectrum done with the back illuminated instrument. The covering fraction is the highest as spected $f = 0.74 \pm 0.07$

5.4.4.2 BeppoSAX dip spectra

We fitted the BeppoSAX observations with the *Partial covering bbody* and *Partial covering diskline* models (see Table 5.6), during dips. The data was fitted throughout the dips (see Fig. 5.28 and Fig. 5.29). These models are based on M.J. Church's (see [112]) study of the source with BeppoSAX. In this paper, only LECS and MECS are in use and different parts of the dip are under study.
In the first BeppoSAX observation (see Fig. 5.28) a possible broad line was observed and modelled with a diskline component at an energy range of 6.2 - 6.6 keV. This line may correspond to a broad iron K_α emission line. This emission line might have been produced in the disc, close to the neutron star and broaded maybe due to relativistic effects, Compton effects or both. No line was observed in the second BeppoSAX observation.

(b) and (c) model	First observation	Second observation
χ^2	1.03	1.08
$n_H\left(10^{22}cm^{-2}\right)$	361.12 ± 961.51	335.02 ± 80.46
kT_{bb}	1.85 ± 3.13	1.07 ± 0.84
$norm_{\ bb}$	0.10 ± 0.01	0.08 ± 0.01
$n_H\left(10^{22}cm^{-2}\right)$	1.3 ± 0.1	0.86 ± 0.10
$n_H\left(10^{22}cm^{-2}\right)$	41 ± 9	20.53 ± 4.74
f	0.89 ± 0.0.3	0.30 ± 0.32
Γ	1.39 ± 0.19	1.46 ± 0.28
E_{CO}	55.01 ± 0.22	56.65 ± 0.37
norm	0.01 ± 0.004	0.01 ± 0.01
Diskline keV	6.34 ± 0.18	– –
Disk Betor	-2.96 ± 1.15	– –
Disk Rin	35.03 ± 34.82	– –

TABLE 5.8: Partial covering BeppoSAX Best fit parameters

The blackbody column density in both BeppoSAX observations are highly increased in comparison with the column densities in the persistent. The blackdoby temperature oscillates from 1.07 to 1.85 from both observations with a Γ of 1.39 and 1.46 respectively. In both cases, spectral hardening is detected above 100 keV.
In both models we obtained a χ^2 of 1.03 and 1.08 respectively.

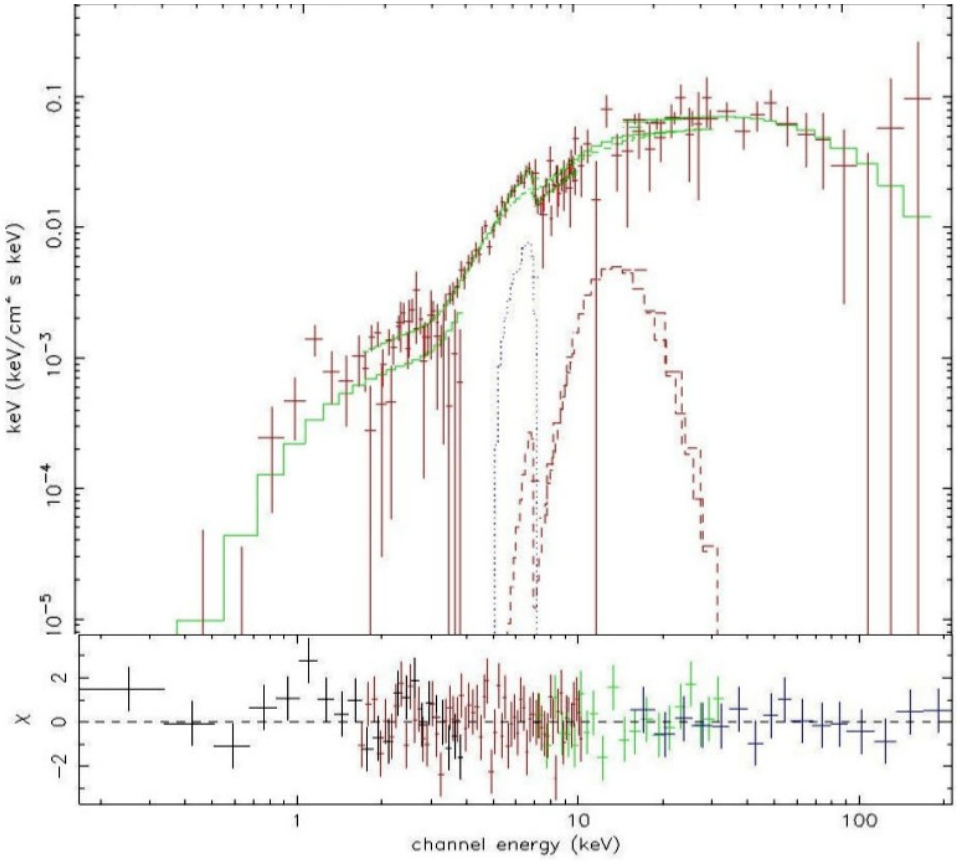

FIGURE 5.28: Unfolded energy spectrum extracted from dip data of the 1st observation BeppoSAX with best fit and residuals using model Partial covering diskline

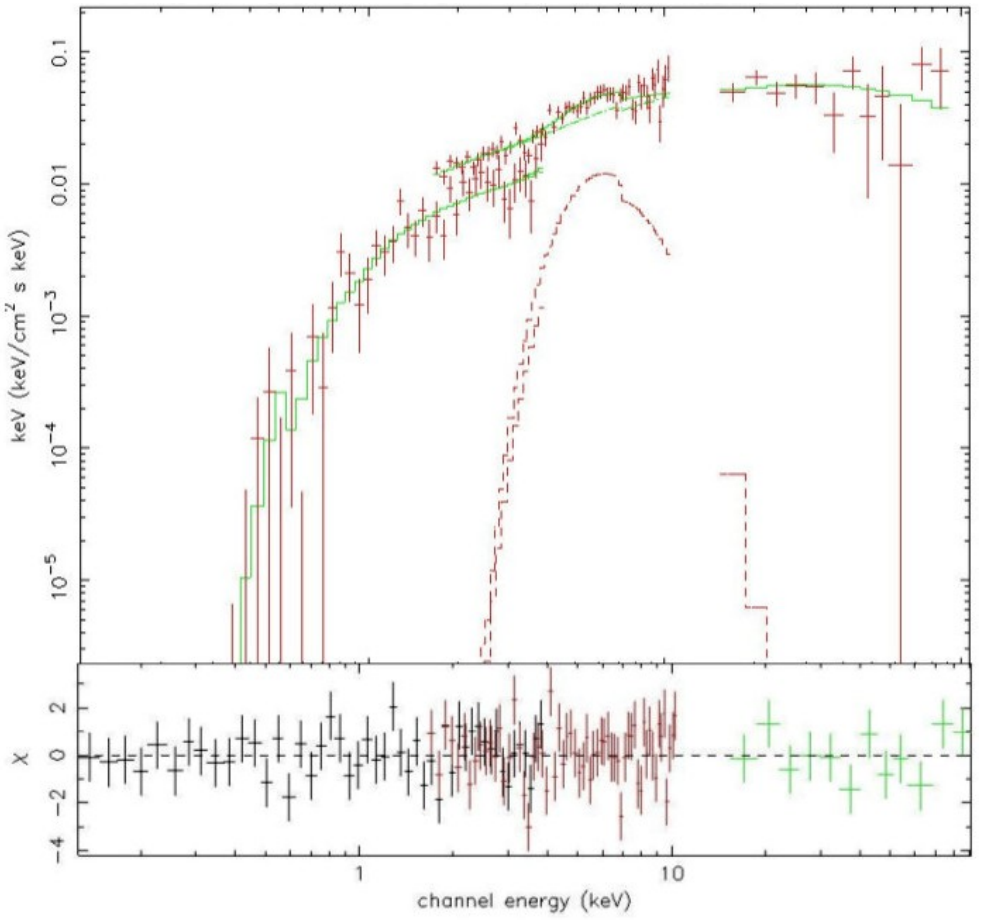

FIGURE 5.29: Unfolded energy spectrum extracted from dip data of the 2nd observation BeppoSAX with best fit and residuals using model Partial covering bbody

From the study of the source spectra with BeppoSAX and Suzaku we can conclude the following: The partial covering approach is well modelled and good fits in all cases are obtained. Consistent covering fraction results are obtained in all cases with high increases of the column density. Only one observation gives rise to an iron line in emission possibly emitted from the interior part of the accretion disc. The 3 dip approach in Suzaku data, rule out any possible bad time selection giving good fits and a higher covering fraction.

Chapter 6

Conclusions

6.1 Conclusions

We analysed data from 4U 1916-053, a LMXB situated in the vicinity of the galactic centre, with Suzaku, BeppoSAX, MAXI and RXTE/ASM observations obtained, performed on 1997 and 2001 for BeppoSAX, 2005 for Suzaku, 2014 for MAXI and a compound of several years for ASM.

For the spectral analysis of the source, BeppoSAX and Suzaku observations were used due to their broad energy range. LECS, MECS, HP, PDS promoted BeppoSAX to be efficient in a range from 0.1 to 220 keV. XIS, PIN and GSO allow Suzaku in a range from 0.1 to 700 keV. Data from both satellites was used and divided into the persistent and dip spectra. A double blackbody was modelled with BeppoSAX data promoting the interpretation of the emission from the source [91]. The spectrum extends to above 200 keV.

For the Suzaku observation, a *simple bbody model* was tried unsuccessfully, with a poor fit and some negative residuals at 6.65 and 6.95 keV. Thanks to the more precise spectroscopic measurements, this gave rise to the observation of two narrow iron lines at 6.65 and 6.94 keV corresponding to Fe XXV and Fe XXVI Kα in the persistent by modelling the data with two gaussians in the respective energy ranges. These line observations confirm previous observations done by XMM and CHANDRA. These absorption lines are produced in a photoionized absorber placed at the edge of the accretion disc, probably the same absorber producing the dips when it is less ionized [110].
A *comptonized model* was used, as in other referenced papers, fitting an observed edge in addition to the two iron lines in absorption, verifying the results [110].

The Dip spectrum was modelled by a "partial covering" scenario in both Suzaku and BeppoSAX observations, corroborating the use of this approach. Spectral hardening was observed in both cases. In one of the BeppoSAX observations, a residual was observed and modelled by a diskline component between 6.2 and 6.6 keV. This possible broad line only appeared in one of the observations of BeppoSAX. This line indicates a possible iron K_α emission, that should be produced near the neutron star surface and broaded due to Compton effects.

A more detailed study thanks to a higher amount of counts during dipping was carried out by Suzaku, focusing in specific dips, obtaining a good fit with the partial covering scenario. No iron line was observed during dips.

From timing analysis, the light curves showed the intensity variation due to the existence of dips in the range of 1-10 keV. For instruments with a higher energy range, the dip feature is either non existing or less apparent. A burst on the Suzaku light curve was recognized. From the display of the light curves from BeppoSAX and Suzaku in different period of time, differences in the dip shape are observed, confirming the variability of dips of this source over time. Color color diagrams were performed with BeppoSAX, RXTE/ASM and MAXI. Unfortunately, due to two edges in the Suzaku data, no reliable color color diagram could be created. From the BeppoSAX observation it could be established that the source was in the banana state, verifying the spectral hardening during dipping from these plots. From the RXTE/ASM data and from comparing all the other color color diagram, the complete atoll behaviour could be verified.

Bibliography

[1] Thales of Miletus. Thales of miletus. *Encyclopedia of Philosophy*, 2014. URL http://www.iep.utm.edu/thales/.

[2] Anaxagoras. Anaxagoras. *Encyclopedia of Philosophy*, 2014. URL http://www.iep.utm.edu/anaxagor/.

[3] Eudoxus. Eudoxus. *Encyclopedia of Philosophy*, 2014. URL http://www.iep.utm.edu.

[4] Encyclopedia Britannica. Aristarchus-of-samos. *Encyclopedia Britannica*, 2014. URL http://www.britannica.com/EBchecked/topic/34377/Aristarchus-of-Samos.

[5] Polaris project. The ptolemaic model. *Polaris project*, 2014. URL http://www.polaris.iastate.edu/EveningStar/Unit2/unit2_sub1.htm.

[6] Nicholas Copernicus. De revolutionibus (on the revolutions). *Copernicus*, 1543. URL http://www.webexhibits.org/calendars/year-text-Copernicus.html.

[7] Galileo project. Kepler. *Galileo project*, 2014. URL http://galileo.rice.edu/sci/kepler.html.

[8] Issac Newton Institute. Issac newton's life. *Mathematical Sciences*, 2014. URL https://www.newton.ac.uk/about/isaac-newton/life.

[9] wolfram. three-body. *wolfram*, 2013. URL http://www.wolframscience.com/reference/notes/972d.

[10] Ana Larson. Identifying elements in the sun using spectral lines. *University of Washington*, 2013. URL http://www.columbia.edu/~vjd1/Solar%20Spectrum%20Ex.html.

[11] N.A.S.A. The electromagnetic spectrum. *NASA*, Feb 2014. URL http://imagine.gsfc.nasa.gov/docs/science/know_l1/emspectrum.html.

[12] Raymond Davies Jr. Exosat. *Nobel Prize*, 2002. URL http://www.nobelprize.org/nobel_prizes/physics/laureates/2002/giacconi-bio.html.

[13] Herbert Friedman Papers. Abstract. *Herbert Friedman Papers*, 2014. URL http://www.amphilsoc.org/mole/view?docId=ead/Mss.Ms.Coll.113-ead.xml.

[14] Joe Tenn. Bruno rossi archive. *Hardvard University Archives*, 2014. URL http://www.phys-astro.sonoma.edu/BruceMedalists/Giacconi/GiacconiRefs.html.

[15] Rosalia Madonia Andrea Santangelo. Fifty years of x-ray astronomy: A look back into the (near) future. *Elsevier*, 2013. URL http://ac.els-cdn.com/S0927650513001631/1-s2.0-S0927650513001631-main.pdf?_tid=5ec7d744-43cb-11e4-a550-00000aacb35f&acdnat=1411550327_47677da716c8894e4c72409369b32990.

[16] N.A.S.A. Uhuru satellite. *N.A.S.A.*, 1972. URL http://heasarc.gsfc.nasa.gov/Images/uhuru/uhuru_weight.gif.

[17] California Science Center. Uhuru. *California Science Center*, 2013. URL https://www.californiasciencecenter.org/Exhibits/AirAndSpace/StarsAndTelescopes/Uhuru/Uhuru.php0.

[18] NASA. Heao ii. *NASA*, 2013. URL http://nssdc.gsfc.nasa.gov/nmc/spacecraftDisplay.do?id=1978-103A.

[19] ESA. Exosat. *ESA*, 2013. URL http://sci.esa.int/exosat/.

[20] ESA. Xmm-newton. *ESA*, 2014. URL http://sci.esa.int/xmm-newton/31249-summary/.

[21] NASA. Fermi. *NASA*, 2014. URL http://www.nasa.gov/mission_pages/GLAST/main/.

[22] LEDEN et EDP sciences. Photoelectric absorption. *EDP science*, 2008. URL http://www.laradioactivite.com/en/site/pages/PhotoElectric_Effect.htm.

[23] DC ciscuits. Kirchhoff laws. *Physics tutorial*, 2014. URL http://www.physics.uoguelph.ca/tutorials/ohm/Q.ohm.KCL.html.

[24] Joern Wilms. Blackbody radiation. *Bamberg*, 2008. URL http://pulsar.sternwarte.uni-erlangen.de/wilms/teach/radproc/radproc0070.html.

[25] Pr. Dr. Andrea Santangelo. Bremmstrahlung. *Uni Tuebingen*, 2008. URL http://astro.uni-tuebingen.de/seminars/scripts/santangelo/Obs_Astro_WS1314/WS_2012_2013_09_Roentgenastronomie_I_HQ.pdf.

[26] Pr. Dr. Werner Vogelsang. Quantenmechanik 1. *Uni Tuebingen*, 2011. URL http://www.tphys.physik.uni-tuebingen.de/~vogelsang/QM1-2011_files/Skript_QM1_SoSe11.pdf.

[27] Steven R. Dabic. Compton scattering and differential cross section. *MIT*, 2014. URL http://www.identicoin.com/PAPERS/Compton.pdf.

[28] Chicago. Compton scattering. *University Chicago*, 2014. URL http://background.uchicago.edu/~whu/courses/ast305_10/ast305_08.pdf.

[29] Pr. Dr. Andrea Santangelo. Compton scattering. *Uni Tuebingen*, 2008. URL http://astro.uni-tuebingen.de/seminars/scripts/santangelo/Obs_Astro_WS1314/WS_2012_2013_09_Roentgenastronomie_I_HQ.pdf.

[30] Longair. Neutron star structure. *Cambridge*, 2006. URL http://www.cambridge.org/us/academic/subjects/astronomy/astrophysics/high-energy-astrophysics-3rd-edition.

[31] CSIRO. Main sequence properties. *Australia Telescope National Facility*, 2006. URL http://www.atnf.csiro.au/outreach/education/senior/astrophysics/stellarevolution_mainsequence.html#mslifespan.

[32] CSIRO. Main sequence stars. *Australia Telescope National Facility*, 2006. URL http://www.atnf.csiro.au/outreach/education/senior/astrophysics/stellarevolution_mainsequence.html#mscno.

[33] Richard Powell. Photoelectric absorption. *Richard Powell*, 2008. URL http://www.atlasoftheuniverse.com/hr.html.

[34] Pr. Dr. Andrea Santangelo. cno and pp cycle. *Uni Tuebingen*, 2008. URL http://astro.uni-tuebingen.de/seminars/scripts/santangelo/Obs_Astro_WS1314/WS_2012_2013_09_Roentgenastronomie_I_HQ.pdf.

[35] Dr. Christopher Palma. Stellar evolutionary tracks in the hr diagram. *Pennsylvania State University*, 2006. URL https://www.e-education.psu.edu/astro801/content/l5_p5.html.

[36] Raymon Davies. P-p cycle. *John A. Dutton education*, 2006. URL https://www.e-education.psu.edu/astro801/content/l5_p4.html.

[37] Borb. Cno cycle. *Wikipedia*, 2006. URL http://en.wikipedia.org/wiki/File:CNO_Cycle.svg.

[38] Elisabeth Howell. Main sequence properties. *Space.com*, 2013. URL http://www.space.com/21640-star-luminosity-and-magnitude.html.

[39] M.S. Longair. High energy astrophysics. *Cambridge*, 2013. URL http://ams.pg.infn.it/~emanuele/lezioni-astrofisica1011/libri%20di%20testo/Physics%20-Longair%20-%20High%20Energy%20Astrophysics%20Vol%201%20%282Nd%20Ed%29.pdf.

[40] F. Zwicky W. Baade. Neutron star structure. *APS journals*, May 1934. URL http://journals.aps.org/pr/abstract/10.1103/PhysRev.46.76.2.

[41] R. Nave. Supernovae. *Hyperphysics*, May 2014. URL http://hyperphysics.phy-astr.gsu.edu/hbase/astro/snovcn.html.

[42] R. Naeye. Fermi. *NASA*, May 2014. URL http://www.nasa.gov/mission_pages/GLAST/science/neutron_stars.html.

[43] Red Orbit. Cen x-1 pulsation. *Red Orbit*, 2007. URL http://www.redorbit.com/media/uploads/2007/08/b07cda65a74dc17b58e562e85c9ee32f1.jpg.

[44] Voigt. Abriss der astronomie. *Wiley-VCH*, 1991. URL http://www.wiley-vch.de/publish/dt/books/ISBN978-3-527-41123-8/.

[45] I. Kreykenbohm. X-ray spectra of highly magnetized neutron stars in binary systems. *AIT*, May 2006. URL https://publikationen.uni-tuebingen.de/xmlui/bitstream/handle/10900/48640/pdf/dissertation.pdf?sequence=1&isAllowed=y.

[46] ESA. Exosat. *ESA*, 2014. URL http://sci.esa.int/exosat/.

[47] Joern Wilms. Cen x-1 pulsation. *Bamberg*, 2008. URL http://pulsar.sternwarte.uni-erlangen.de.

[48] Gianluca Israel. Accretion. *Gianluca*, 1997. URL http://www.mporzio.astro.it/gianluca/phdthesis/node10.html.

[49] Prof. Dr. Santangelo. Roche lobe potential. *Uni Tuebingen*, 2008. URL http://astro.uni-tuebingen.de/seminars/scripts/santangelo/.

[50] James Wittke. Roche lobe overflow. *nau*, 2006. URL https://www4.nau.edu/meteorite/Meteorite/Book-GlossaryR.html.

[51] Joern Wilms. X-ray binaries. *Bamberg*, 2008. URL http://pulsar.sternwarte.uni-erlangen.de/wilms/teach/xrb/xrbchap6toc.html.

[52] Joern Wilms. Z source ccd. *Bamberg*, 2008. URL http://pulsar.sternwarte.uni-erlangen.de/wilms/teach/xrb/xrb0167.html.

[53] Y.-J. Lei, S. Zhang, J.-L. Qu, H.-L. Yuan, Y.-N. Wang, Y.-Q. Dong, H.-T. Zhang, Z.-B. Li, C.-M. Zhang, and Y.-H. Zhao. The properties of cross-correlation and spectra of the low-mass x-ray binary 4u 1608-52. *arXiv*, mar 2014. URL http://adsabs.harvard.edu/abs/2014AJ....147...67L.

[54] Joern Wilms. Atoll source ccd. *Bamberg*, 2008. URL http://pulsar.sternwarte.uni-erlangen.de/wilms/teach/xrb/xrb0169.html.

[55] L. Parmar. Bepposax observation of the eclipsing dipping x-ray binary x 1658-298. *AA*, 2001. URL http://pulsar.sternwarte.uni-erlangen.de/wilms/teach/xrb/xrbchap6toc.html.

[56] L. Boirin. Roche lobe potential. *Strasbourg Observatorium*, 2009. URL http://www.mssl.ucl.ac.uk/~gbr/workshop3/papers/mssl09boirin.pdf.

[57] J. Wilms. X-ray binaries. *Bamberg*, 2001. URL http://pulsar.sternwarte.uni-erlangen.de/wilms/teach/xrb/xrbchap6toc.html.

[58] Sudip Bhattacharyya. Measurement of neutron star parameters, a review method for low-mass x-ray binaries. *inspire*, 2002. URL http://inspirehep.net/record/842548/plots?ln=en.

[59] ASI. Bepposax satellite. *ASI*, 2014. URL http://www.asi.it/en/activity/navigation.

[60] NSO. Netherlands space office. *NSO*, 2014. URL http://www.spaceoffice.nl/.

[61] Alenia Spazio. Thales. *Alenia Spazio*, 1997. URL https://www.thalesgroup.com/en/worldwide/space?LangType=2057.

[62] ASDC. Bepposax satellite. *ASDC*, 1997. URL http://www.asdc.asi.it/bepposax/sax_orbit.html.

[63] NASA. Bepposax payload. *NASA*, 2001. URL http://heasarc.gsfc.nasa.gov/docs/sax/gallery/sax_inst.html.

[64] ASDC. Bepposax lecs detector. *ASDC*, 2003. URL http://www.asdc.asi.it/bepposax/lecs.html.

[65] ASDC. Bepposax mecs detector. *ASDC*, 2001. URL http://www.asdc.asi.it/bepposax/mecs.html.

[66] ASDC. Hp detector. *ASDC*, 1997. URL http://www.asdc.asi.it/bepposax/hpgspc.html.

[67] ASDC. Bepposax pds. *ASDC*, 2001. URL http://www.asdc.asi.it/bepposax/pds.html.

[68] ASDC. Pds detector. *ASDC*, 1997. URL http://www.asdc.asi.it/bepposax/pds.html.

[69] NSO. Netherlands space office. *NSO*, 2014. URL http://www.isas.jaxa.jp/e/enterp/missions/asca/.

[70] JAXA. Japanese aerospace. *JAXA*, 2014. URL http://www.isas.jaxa.jp/e/index.shtml.

[71] NASA. Suzaku satellite. *NASA*, 2005. URL http://www.nasa.gov/mission_pages/astro-e2/main/.

[72] NASA. Suzaku xis detector. *NASA*, 2005. URL http://xmm2.esac.esa.int/external/xmm_sw_cal/icwg/presentations/Suzaku_overview_XIS.pdf.

[73] NASA. Suzaku hxd detector. *NASA*, 2005. URL http://xmm2.esac.esa.int/external/xmm_sw_cal/icwg/presentations/Suzaku_overview_XIS.pdf.

[74] NASA. Suzaku xrt detector. *NASA*, 2005. URL http://xmm2.esac.esa.int/external/xmm_sw_cal/icwg/presentations/Suzaku_overview_XIS.pdf.

[75] JAXA. Xrt failure. *JAXA*, 2001. URL http://www.isas.jaxa.jp/j/snews/2006/0126.shtml.

[76] JAXA. Xis2. *JAXA*, 2006. URL http://heasarc.gsfc.nasa.gov/docs/suzaku/news/xis2.html.

[77] JAXA. Maxi instrument. *JAXA*, 2009. URL http://www.nasa.gov/mission_pages/station/research/experiments/603.html.

[78] JAXA. Maxi instrument. *JAXA*, 2009. URL http://kibo.jaxa.jp/en/experiment/ef/maxi/.

[79] JAXA. Maxi instrument. *JAXA*, 2009. URL http://www.hp.phys.titech.ac.jp/fermi/presentations/TM_Maxi.pdf.

[80] RXTE. Rxte. *NASA*, 2014. URL http://heasarc.gsfc.nasa.gov/docs/xte/xte_1st.html.

[81] RXTE. Rxte virtual tour. *RXTE*, 2014. URL http://cass.ucsd.edu/hexte/hexte/tour/rxte_spacecraft.html.

[82] Ş. Balman. A study of the low-mass x-ray binary dip sources xb 1916 - 053, xb 1323 - 619, x 1624 - 490 and 4u 1746 - 371 observed with integral. *Astrophysical journal*, 138(0904.3432):50–62, Jul 2009. URL http://adsabs.harvard.edu/abs/2009AJ....138...50B.

[83] D. Galloway. Thermonuclear bursts from millisecond x-ray pulsars. *RXTE proposal*, 120(910507):c269, Jun 2005. URL http://adsabs.harvard.edu/abs/1996A%26AS..120C.269B.

[84] STR. 4u 1916-053. *SIMBAD*, 2014. URL http://cds.u-strasbg.fr/cgi-bin/Dic-Simbad?3A.

[85] J. H. Swank, R. E. Taam, and N. E. White. The mxb1916-053/4u1915-05: Burst properties and constraints on a 50 minute binary secondary. *Astrophysical journal*, 83(3):34862, Aug 1983. URL http://adsabs.harvard.edu/abs/1983STIN...8334862S.

[86] A. P. Smale, K. O. Mason, N. E. White, and M. Gottwald. The evolution of very low mass stars. *Tanaka*, 311(2S):201–204, Jun 1988. URL http://adsabs.harvard.edu/abs/1988pnsb.conf..201S.

[87] L. A. Nelson, S. A. Rappaport, and P. C. Joss. The evolution of very low mass stars. *astrophysical ournal*, 311(10.1086):226–240, Jun 1986. URL http://adsabs.harvard.edu/abs/1986ApJ...311..226N.

[88] D. Barret, J. E. Grindlay, M. Strickman, and G. Vedrenne. Cgro/osse observations of the x-ray burster 4u 1915-05 (xb 1916-053). *Astrophysical journal*, 120 (10.1016):c269, Jun 1996. URL http://adsabs.harvard.edu/abs/1996A%26AS..120C.269B.

[89] M. Falanga, L. Kuiper, J. Poutanen, D. K. Galloway, E. Bozzo, A. Goldwurm, W. Hermsen, and L. Stella. Accreting millisecond x-ray pulsars: 10 years of integral observations. *astrophysical journal*, 400(1302.2843):555, Feb 2013. URL http://adsabs.harvard.edu/abs/2013arXiv1302.2843F.

[90] A. P. Smale, K. Mukai, O. R. Williams, M. H. Jones, and R. H. D. Corbet. Ginga observations of the dipping low-mass x-ray binaries xb 1916-053 and exo 1748-676. *astrophysical journal*, 400(10.1086):330–343, Nov 1992. URL http://adsabs.harvard.edu/abs/1992ApJ...400..330S.

[91] E. Göğüş, M. A. Alpar, and M. Gilfanov. Is the lack of pulsations in low-mass x-ray binaries due to comptonizing coronae? *Astrophysical journal*, 659(3):1236–1239, April 2007. URL http://adsabs.harvard.edu/abs/2007ApJ...659..580G.

[92] JAXA. Xspec user guide. *JAXA*, 311(2S):300, Jun 1988. URL http://maxi.riken.jp/top/index.php?cid=1&jname=J1918-052.

[93] Parmar. Church. Progressive covering in dipping and comptonization in the spectrum of xb1916-053 from the bepposax observation. *arXiv:astro-ph/9806223*, 311 (2S):299, Jun 1988. URL http://arxiv.org/abs/astro-ph/9806223.

[94] L. Boirin, A. N. Parmar, D. Barret, and S. Paltani. Discovery of x-ray absorption lines from the low-mass x-ray binaries 4u 1916-053 and x 1254-690 with xmm-newton. *Astrophysical journal*, 132(10.1016):506–511, Jun 2004. URL http://adsabs.harvard.edu/abs/2004NuPhS.132..506B.

[95] NASA. Software. *NASA*, 2014. URL http://heasarc.gsfc.nasa.gov/docs/software/lheasoft/.

[96] R. Morley. Suzaku. *Royal Astronomical Society*, 302:593–598, 1999. URL http://adsabs.harvard.edu/full/1999MNRAS.302..593M.

[97] JAXA. Maxi all sky monitor. *JAXA*, 311(1):1, Jun 2013. URL http://maxi.riken.jp/top/.

[98] Guido van Rossum. Python programming language. *python*, 311(1):1, Jun 2013. URL https://www.python.org/.

[99] Masaru Matsuoka. The maxi mission on the iss: Science and instruments for monitoring all sky x-ray images. *arXiv.org*, 2014. URL http://arxiv.org/abs/0906.0631.

[100] NASA. Software. *NASA*, 2013. URL http://heasarc.gsfc.nasa.gov/docs/suzaku/analysis/abc/.

[101] IDL. Software. *IDL*, 2013. URL http://www.exelisvis.com/ProductsServices/IDL.aspx.

[102] MIT. Light curves. *ASM*, 2013. URL http://xte.mit.edu/ASM_lc.html.

[103] NASA. Binary system. *NASA*, 311(1):1, Jun 2014. URL http://heasarc.gsfc.nasa.gov/docs/software/lheasoft/.

[104] JAXA. Xis detectors. *JAXA*, 311(1):1, Jun 2013. URL http://www.astro.isas.jaxa.jp/suzaku/doc/suzaku_td/node10.html#SECTION00101300000000000000.

[105] NASA. Suzaku abc guide. *NASA*, 311(1):1, Jun 2013. URL http://heasarc.gsfc.nasa.gov/docs/suzaku/analysis/abc/.

[106] Slawomir Suchy. Suzaku. *IAAT*, 2014. URL s.suchy@gmx.de.

[107] NASA. Suzaku abc guide. *NASA*, 311(1):1, Jun 2013. URL http://www.asdc.asi.it/bepposax/software/.

[108] NASA. Xspec user guide. *NASA*, 311(2S):300, Jun 2014. URL http://heasarc.gsfc.nasa.gov/docs/software/lheasoft/ftools/xselect/xselect.html.

[109] M.J. Church. The nature of the island and banana states in atoll sources and a unified model for low-mass x-ray binaries. *arxviv*, 2013. URL http://arxiv.org/pdf/1312.1823.pdf.

[110] L. Boirin, A. N. Parmar, D. Barret, S. Paltani, and J. E. Grindlay. Discovery of x-ray absorption features from the dipping low-mass x-ray binary xb 1916-053 with xmm-newton. *astrophysical journal*, 311(418):1061–1072, May 2004. URL http://adsabs.harvard.edu/abs/2004A%26A...418.1061B.

[111] A. N. Parmar. Periodic dips in x-ray binaries. *astrophysical journal*, 106(106):1061–1072, May 1986. URL http://adsabs.harvard.edu/abs/1986Obs...106....7P.

[112] M. J. Church, A. N. Parmar, M. Balucinska-Church, T. Oosterbroek, D. dal Fiume, and M. Orlandini. Progressive covering in dipping and comptonization in the spectrum of xb 1916-053 from the bepposax observation. *aap*, 338(106):556–562, Oct 1998. URL http://adsabs.harvard.edu/abs/1998A%26A...338..556C.